



Defense Threat Reduction Agency  
8725 John J. Kingman Road, MS  
6201 Fort Belvoir, VA 22060-6201



DTRA-TR-13-1

# TECHNICAL REPORT

## Silicon-Based Nanoscale Composite Energetic Materials

Approved for public release, distribution is unlimited.

February 2013

HDTRA1-08-1-0006

Steven F. Son et al.

Prepared by:  
Purdue University  
130 Chaffee Hall  
500 Allison Road  
West Lafayette, IN 47907

**DESTRUCTION NOTICE:**

Destroy this report when it is no longer needed.  
Do not return to sender.

PLEASE NOTIFY THE DEFENSE THREAT REDUCTION  
AGENCY, ATTN: DTRIAC/ J-3 ONIUI , 8725 JOHN J. KINGMAN ROAD,  
MS-6201, FT BELVOIR, VA 22060-6201, IF YOUR ADDRESS  
IS INCORRECT, IF YOU WISH THAT IT BE DELETED FROM THE  
DISTRIBUTION LIST, OR IF THE ADDRESSEE IS NO  
LONGER EMPLOYED BY YOUR ORGANIZATION.

<b>REPORT DOCUMENTATION PAGE</b>			<i>Form Approved</i> <b>OMB No. 0704-0188</b>	
Public reporting burden for this collection of information is estimated to average 1 hour per response, including the time for reviewing instructions, searching existing data sources, gathering and maintaining the data needed, and completing and reviewing this collection of information. Send comments regarding this burden estimate or any other aspect of this collection of information, including suggestions for reducing this burden to Department of Defense, Washington Headquarters Services, Directorate for Information Operations and Reports (0704-0188), 1215 Jefferson Davis Highway, Suite 1204, Arlington, VA 22202-4302. Respondents should be aware that notwithstanding any other provision of law, no person shall be subject to any penalty for failing to comply with a collection of information if it does not display a currently valid OMB control number. <b>PLEASE DO NOT RETURN YOUR FORM TO THE ABOVE ADDRESS.</b>				
<b>1. REPORT DATE (DD-MM-YYYY)</b> 00-02-2013		<b>2. REPORT TYPE</b> Technical		<b>3. DATES COVERED (From - To)</b> Jan. 2008 - July 2012
<b>4. TITLE AND SUBTITLE</b> Silicon-Based Nanoscale Composite Energetic Materials		<b>5a. CONTRACT NUMBER</b> HDTRA1-08-1-0006		
		<b>5b. GRANT NUMBER</b> 102922		
		<b>5c. PROGRAM ELEMENT NUMBER</b>		
<b>6. AUTHOR(S)</b> Steven F. Son, Richard A. Yetter, and Alexander S. Mukasyan		<b>5d. PROJECT NUMBER</b>		
		<b>5e. TASK NUMBER</b>		
		<b>5f. WORK UNIT NUMBER</b>		
<b>7. PERFORMING ORGANIZATION NAME(S) AND ADDRESS(ES)</b> Purdue University 130 Chaffee Hall 500 Allison Road West Lafayette, IN 47907		<b>8. PERFORMING ORGANIZATION REPORT NUMBER</b>		
<b>9. SPONSORING / MONITORING AGENCY NAME(S) AND ADDRESS(ES)</b> Defense Threat Reduction Agency 8725 John J. Kingman Road STOP 6201 Fort Belvoir, VA 22060		<b>10. SPONSOR/MONITOR'S ACRONYM(S)</b> DTRA		
		<b>11. SPONSOR/MONITOR'S REPORT NUMBER(S)</b> DTRA-TR-13-1		
<b>12. DISTRIBUTION / AVAILABILITY STATEMENT</b> Approved for public release; distribution is unlimited.				
<b>13. SUPPLEMENTARY NOTES</b>				
<b>14. ABSTRACT</b> The primary goal of this effort is to develop a fundamental understanding of silicon-based reactives, which are relatively unstudied reactive systems so that applications can be pursued. During this final year (project begun Jan. 2008), we have made significant progress especially in the following areas: 1) optimizing the nano silicon synthesis, 2) finalizing our doped silicon work, 3) using multiple-scale structures in nanoporous silicon structure to control reaction, and 4) showing that mechanically activated Si-Al reactives show significant promise. We will emphasize these results in this final report. Previous year reports and publications have more details on previous work.				
<b>15. SUBJECT TERMS</b> silicon reactives, energetic materials, nanoenergetics				
<b>16. SECURITY CLASSIFICATION OF:</b>			<b>17. LIMITATION OF ABSTRACT</b> UU	<b>18. NUMBER OF PAGES</b> 34
<b>a. REPORT</b> Unclassified	<b>b. ABSTRACT</b> Unclassified	<b>c. THIS PAGE</b> Unclassified		
				<b>19b. TELEPHONE NUMBER (include area code)</b> 765-494-8208

# CONVERSION TABLE

Conversion Factors for U.S. Customary to metric (SI) units of measurement.

MULTIPLY → BY → TO GET  
TO GET ← BY ← DIVIDE

angstrom	1.000 000 x E -10	meters (m)
atmosphere (normal)	1.013 25 x E +2	kilo pascal (kPa)
bar	1.000 000 x E +2	kilo pascal (kPa)
barn	1.000 000 x E -28	meter <sup>2</sup> (m <sup>2</sup> )
British thermal unit (thermochemical)	1.054 350 x E +3	joule (J)
calorie (thermochemical)	4.184 000	joule (J)
cal (thermochemical/cm <sup>2</sup> )	4.184 000 x E -2	mega joule/m <sup>2</sup> (MJ/m <sup>2</sup> )
curie	3.700 000 x E +1	*giga bacquerel (GBq)
degree (angle)	1.745 329 x E -2	radian (rad)
degree Fahrenheit	$t_k = (t^{\circ}f + 459.67)/1.8$	degree kelvin (K)
electron volt	1.602 19 x E -19	joule (J)
erg	1.000 000 x E -7	joule (J)
erg/second	1.000 000 x E -7	watt (W)
foot	3.048 000 x E -1	meter (m)
foot-pound-force	1.355 818	joule (J)
gallon (U.S. liquid)	3.785 412 x E -3	meter <sup>3</sup> (m <sup>3</sup> )
inch	2.540 000 x E -2	meter (m)
jerk	1.000 000 x E +9	joule (J)
joule/kilogram (J/kg) radiation dose absorbed	1.000 000	Gray (Gy)
kilotons	4.183	terajoules
kip (1000 lbf)	4.448 222 x E +3	newton (N)
kip/inch <sup>2</sup> (ksi)	6.894 757 x E +3	kilo pascal (kPa)
ktap	1.000 000 x E +2	newton-second/m <sup>2</sup> (N-s/m <sup>2</sup> )
micron	1.000 000 x E -6	meter (m)
mil	2.540 000 x E -5	meter (m)
mile (international)	1.609 344 x E +3	meter (m)
ounce	2.834 952 x E -2	kilogram (kg)
pound-force (lbs avoirdupois)	4.448 222	newton (N)
pound-force inch	1.129 848 x E -1	newton-meter (N-m)
pound-force/inch	1.751 268 x E +2	newton/meter (N/m)
pound-force/foot <sup>2</sup>	4.788 026 x E -2	kilo pascal (kPa)
pound-force/inch <sup>2</sup> (psi)	6.894 757	kilo pascal (kPa)
pound-mass (lbm avoirdupois)	4.535 924 x E -1	kilogram (kg)
pound-mass-foot <sup>2</sup> (moment of inertia)	4.214 011 x E -2	kilogram-meter <sup>2</sup> (kg-m <sup>2</sup> )
pound-mass/foot <sup>3</sup>	1.601 846 x E +1	kilogram-meter <sup>3</sup> (kg/m <sup>3</sup> )
rad (radiation dose absorbed)	1.000 000 x E -2	**Gray (Gy)
roentgen	2.579 760 x E -4	coulomb/kilogram (C/kg)
shake	1.000 000 x E -8	second (s)
slug	1.459 390 x E +1	kilogram (kg)
torr (mm Hg, 0° C)	1.333 22 x E -1	kilo pascal (kPa)

\*The bacquerel (Bq) is the SI unit of radioactivity; 1 Bq = 1 event/s.

\*\*The Gray (GY) is the SI unit of absorbed radiation.

**Objective:** The primary goal of this effort is to develop a fundamental understanding of silicon-based reactives, which are relatively unstudied reactive systems so that applications can be pursued. Questions to be addressed include: 1) Can fluorinated self-assembled monolayers be successfully bonded to silicon? 2) Which oxidizers and mixture ratios produce the optimal performance in terms of propagation rate, gas/pressure produced, and heat produced? 3) Why are they optimum? 4) What controls the sensitivity of the composite? 5) How can these systems be simply modeled so that they can eventually be applied to counter WMD applications? The extended work is primarily focused on synthesizing, scaling, and characterizing nanoscale silicon; and characterizing these materials.

**Status of Effort:** During this final year (project begun Jan. 2008), we have made significant progress especially in the following areas: 1) optimizing the nano silicon synthesis, 2) finalizing our doped silicon work, 3) using multiple-scale structures in nanoporous silicon structure to control reaction, and 4) showed that mechanically activated Si-Al reactives show significant promise. We will emphasize these results in this final report. Previous year reports and publications have more details on previous work.

**Personnel Supported:** This project partially supported three faculty members (Richard Yetter, Alex Mukasyan and Steven Son). Two graduate students (one at Purdue and one at Penn State) and a postdoc (ND) are also partially funded. One undergraduate was partially funded by this project as part of the Summer Undergraduate Research Fellowship (SURF) at Purdue. One undergraduate student was supported at Penn State.

**Publications:** Work has been presented in several conference papers/presentations this final year (>4/>6) and six publications are in various stages of review and publication with several more in preparation or submitted. One patent disclosure has been submitted. We plan to submit another patent disclosure in the next few weeks.

**Interactions/Transitions:** We have continued a collaborative relationship with Los Alamos National Laboratory, who also has had other DTRA funding.

**New Discoveries, Inventions, or Patent Disclosures:** Synthesis of nano silicon has been submitted for a patent disclosure. We plan to submit another on mechanically activated Al-Si reactives.

**Honors/Awards:** PI was also named a Purdue University Scholar (2010-15).



## Accomplishments and New Findings

We have been examining the potential of silicon as a fuel ingredient in energetic materials and combustion systems. During the past reporting period, we have concentrated on: 1) optimizing the nano silicon synthesis, 2) finalizing our doped silicon work, 3) using multiple-scale structures in nanoporous silicon structure to control reaction, and 4) showed that mechanically activated Si-Al reactives show significant promise. We will emphasize these results in this final report. Previous year reports and publications have more details on previous work.

## Synthesis, Scale-up, and Characterization of nano silicon

### Background

Silicon has a long history as a reactive fuel in pyrotechnic applications such as delay and primer compositions, near infrared illuminants, and smoke formulations [1]. However, while there has been significant efforts to study micron sized silicon powders in energetic compositions [2-9], relatively little work has focused on the performance enhancement that nanoscale silicon powders (nSi) may provide [10-13]. Increasing the surface area of reactive fuels by either size reduction (e.g., aluminum nanopowder (nAl)) or by chemical processing (e.g., porous silicon (PSi)) has been shown to increase reactivity, lower melting and ignition temperatures, and increase the intimacy of mixing [14-16]. When compared to nAl, nanoscale silicon has several characteristics that have driven current research. Silicon has a smaller passivation layer thickness than aluminum (~1 nm as opposed to ~3-6 nm) [14, 17] which can significantly increase active content and suggests that it may have better aging properties, high predicted flame temperatures when mixed with various oxidizers [13], and surface functionalization of silicon wafers and powders is easily realized [18].

The surface area induced performance enhancement for PSi wafers and powders has been shown to be significant [12, 19-21]. For example, PSi wafer propagation velocities in excess of 6000 m/s have been reported [21] and a variety of oxidants have been explored [20]. However, significant drawbacks to PSi include the difficulty of controlling the stoichiometry and successfully filling the pores. Clément *et al.* [20] have reported that their highest achieved PSi filling factor is only 50%. Because of this, PSi wafer research does not allow for systematic investigations into the effect of Si particle characteristics, such as SSA, oxygen content, and particle size. Therefore, in order to determine which characteristics most influence silicon combustion, silicon powders are a more logical choice.

Recently, Thiruvengadathan *et al.* [10] investigated the combustion of various nSi powders (commercial spherical nanoparticles and high aspect ratio silicon nanowires and nanotubes; both neat and hydrogen-terminated) with nanostructured sodium perchlorate ( $\text{NaClO}_4$ ). Their work showed increased combustion performance achieved through hydrogen-terminated silicon surfaces (surface functionalization) and also indicated that shorter Si nanowires and nanotubes (with constant diameter) yielded faster burning rates, many of which were faster than spherical nSi powder. For commercial nSi powder, Mason *et al.* [11] have reported screening experiments for several oxidizers. Their thermochemical predictions indicate that polytetrafluoroethylene (PTFE) has the highest predicted combustion temperatures of any oxidizer studied at 3531 K, which suggests that the Si/PTFE system is of particular interest to investigate. Over the past few years, a few studies for Si/PTFE, both micron-scale [22, 23] and nano-scale [13], have been reported. However, those studies have only focused on external characteristics (i.e., oxidizer, equivalence ratio, pressure, etc.), but did not address changes in nSi powder characteristics (i.e., morphology, SSA, oxygen content, etc.). There are several reasons for this including cost (nSi is relatively expensive), the quality has been variable, and limited morphologies are available.



While several lab scale methods for producing nSi powders are reported such as chemical reduction [24-26] and self-propagating high-temperature synthesis (SHS) [27], the resulting powders have not been widely explored as a reactive fuel. In a conventional SHS scheme, a heterogeneous exothermic mixture of solid powders is pressed into a pellet and ignited at one end, followed by a high-temperature combustion wave front that propagates through the reactive material, converting the precursors to the desired products. The unique characteristics of this method include: (i) short synthesis duration; (ii) great energy efficiency, since the system's internal chemical energy is used for propagation of the combustion wave; (iii) simple equipment requirements; and (iv) the ability to produce high purity products with unique properties, since the high combustion temperatures generally burn off most impurities. While a SiO<sub>2</sub>/Mg SHS reaction offers a fast, easy, energy-efficient route to nSi synthesis, thermodynamic calculations predict that the adiabatic temperature is ~2200 K, which is higher than the melting point of silicon (1687 K). This implies that as-synthesized silicon will further melt (i.e., sintering effect) and thus will not be able to preserve its nanostructure.

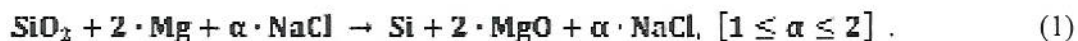
One method recently explored for overcoming this is a modified SHS approach, termed salt-assisted combustion synthesis (SACS) [28]. In a SACS process, the SHS reactive mixture is combined with alkali metal halides (inert material to the investigated system) in order to significantly reduce the combustion temperature, thus keeping the as-synthesized nanostructure. The SACS method allows for nSi powder production with simplicity, higher production rates, easy stoichiometric control, and energy-efficiency.

In this study we utilize the SACS method for the production of various Si powders and compare combustion performance to that of several commercially available powders. Specifically, the Si/PTFE system was investigated. Silicon powder characteristics (e.g., SSA, oxygen content, morphology, and dominant particle size and distribution) of both the commercial and SACS powders were quantified by particle size analysis and scanning electron microscopy/energy dispersive spectroscopy. Combustion temperatures, spectral intensities, and effective emissivities were interpolated from visual (VIS) and infrared (IR) spectroscopy and burning rates were measured from videography of pellet deflagration. Conclusions are drawn from the experimental results indicating the dominant material characteristic controlling burning rate, combustion temperature, and spectral intensity.

## Experimental Methods and Procedures

### SACS PSi Synthesis and Characterization

Reactive mixtures of Mg (99.8 % purity, mean particle size  $d \leq 44 \mu\text{m}$ , Alfa Aesar, USA), SiO<sub>2</sub> (99.5 %,  $d \leq 44 \mu\text{m}$ , Cerac, USA), and NaCl (Alfa Aesar, USA) were chosen for the SACS reaction:



All powders were thoroughly mixed in an ethanol bath (2:1 wt.%, ethanol:mixture) with zirconium oxide (ZrO<sub>2</sub>) milling balls (2:1 wt.%, ball:mixture) for 6 hours, followed by drying in a temperature controlled oven at 353 K for 12 hours. All powders utilized in this work were used as-received. There were no further powder purification treatments prior to reaction. SEM images of the raw materials used in the SACS process are provided as *Figure 1*.



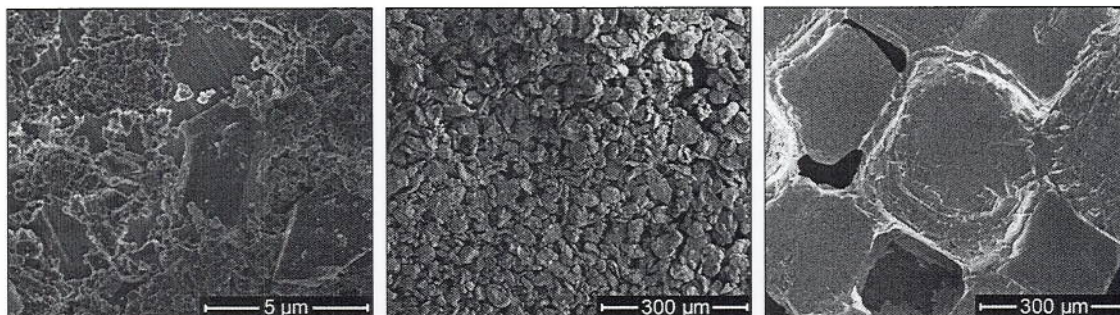


Figure 1. Raw powders used in SACS synthesis process. Left to Right:  $\text{SiO}_2$ , Mg, NaCl.

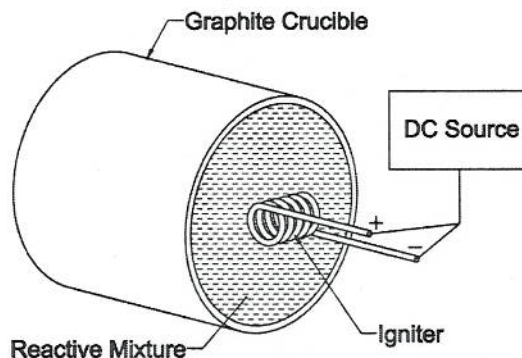
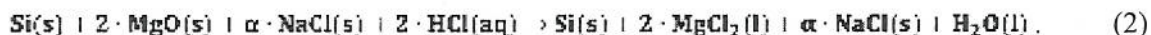


Figure 2. Schematic representation of the experimental assembly.

A schematic representation of the experimental assembly is shown in Figure 2. The  $\text{SiO}_2/\text{Mg}/\alpha\text{NaCl}$  exothermic mixture was placed in a graphite crucible (2" O.D.  $\times$  1.875" I.D.  $\times$  2" Deep) and the crucible was inserted into a cylindrical steel reactor (10" O.D.  $\times$  9" I.D.  $\times$  2 ft length). The reactor was sealed, evacuated to  $10^{-3}$  atm, and then purged with argon gas (99.998 % purity, Praxair Distribution Inc., USA) up to the desired pressure (1-30 atm). The combustion process was initiated by passing a DC pulse (10 A at 20 V) through a tungsten wire located close to the powder surface in the graphite sleeve. The pulse was turned off immediately after reaction initiation. A combustion wave propagated along the sample volume, converting the precursors into the final products. Following the SACS reaction, all materials were cooled in the reactor for 4 hours. The as-synthesized product was then collected for hydrometallurgical treatments.

All as-synthesized products were ground and put into a beaker with different diluted concentrations (5–30 %) of hydrochloric acid (36 %, Alfa Aesar, USA). A stirring bar was placed in the solution, and the MgO products were leached for several hours without any additional heating according to the reaction:



During the leaching process pH test-paper was utilized as an indicator for an acidic environment. In some cases an additional leaching process was carried out with a 100 ml 5% diluted hydrofluoric acid (49 %, Fisher Scientific) in a 250 ml plastic flask with a stirring bar at 323 K for 2 hours. The as-synthesized materials were then subjected to a filtering process. Deionized (DI) water was used to neutralize the acidic Si solution until the pH paper indicated neutral condition. The collected powders were then dried in a fume hood at atmospheric conditions for 12 hours.

Three PSi samples were synthesized using the SACS method in order to characterize the combustion performance of SACS PSi. The three samples were labeled SACS#1-3 and varied only in



hydrometallurgical treatments. All samples were synthesized according to reactions (1) and (2) with  $\alpha=1.0$ . The hydrometallurgical treatments used in SACS#1-3 were: 5% HCl concentration; 5% HCl concentration, with additional multi-acid treatments; and 30% HCl concentration respectively. Material characteristics of the synthesized PSi powder were analyzed using a variety of techniques. BET specific surface area was measured on a Coulter SA3100 analyzer at 77 K, which used nitrogen as the adsorbent gas. The PSi powder was vacuum outgassed at 298 K for 4 hours before SSA measurement. Microstructural morphologies were examined by a field emission scanning electron microscope (SEM) and scanning transmission electron microscope (Magellan 400, FEI, USA). The phase composition of the material was determined before SACS, after SACS, and after the hydrometallurgical treatment by a X-ray diffraction (XRD) analyzer (Scintag, X1 Advanced Diffraction System, Scintag Inc., USA) operated at 40 kV and 30 mA. The XRD recorded step-scan data (step size of  $0.02^\circ$  and counting time of 0.5 s) for the angular range  $20^\circ$ – $80^\circ$ . The PSi purity (i.e. %O<sub>2</sub>) was determined by (i) energy dispersive X-ray spectroscopy (EDS) (INCAx-sight Model 7636; Oxford Instruments, USA) and (ii) an inert gas fusion method in the Leco facility (MI, USA). Particle size distributions of all as-synthesized nSi powders was also completed. As Vesta PSi-E3 and all SACS PSi powders are nominally micron sized, a Malvern Mastersizer 2000 HydroµP was used to determine the particle size distribution. A Malvern Zetasizer Nano Z was used to determine particle sizing of the US-Nano and American Elements nSi powders. De-ionized water was used as the medium for measurements conducted with the Mastersizer and ethanol was used for Zetasizer measurements.

#### SiTV Sample Preparation

The six nSi types used in this study were: Vesta Ceramics PSi-E3, 5 nm pore diameter; US Research Nanomaterials, Inc. (US-Nano), nominally 30-50 nm; American Elements (AE), nominally 5-25 nm; and SACS#1-3. The oxygen content (by EDS), BET specific surface area (SSA), and morphology of these powders are presented in Table 1. Vesta PSi-E3 is nano-porous morphology, and was synthesized by etching high-purity, micron silicon particles with a nitric acid- hydrofluoric acid mixture as described by Farrell *et al.* [29]. This process produces a micron-scale particle that is fully covered by ~5 nm pores. US-Nano nSi is laser synthesized from high-purity silane gas in an argon environment. This process yields discrete, spherical nanoparticles. All SACS nSi types are aggregates of small, spherical nanoparticles surrounding larger, honeycomb particles. Typical SEM images for each nSi type are presented in *Figure 3*.

*Table 1. nSi Material Properties.*

nSi Number	Silicon Type	% O <sub>2</sub> (by EDS)	BET Specific Surface Area [m <sup>2</sup> /g]	Morphology
1	Vesta PSi-E3	5.1	134	Nano-Porous
2	US Research Nanomaterials	2.4	25	Spherical
3	American Elements	22	15	Spherical
4	SACS#1	3-4	46	Nano-Porous*
5	SACS#2	0.3	25	Nano-Porous*
6	SACS#3	14-15	230	Nano-Porous*

\* Aggregates of spherical nSi particles



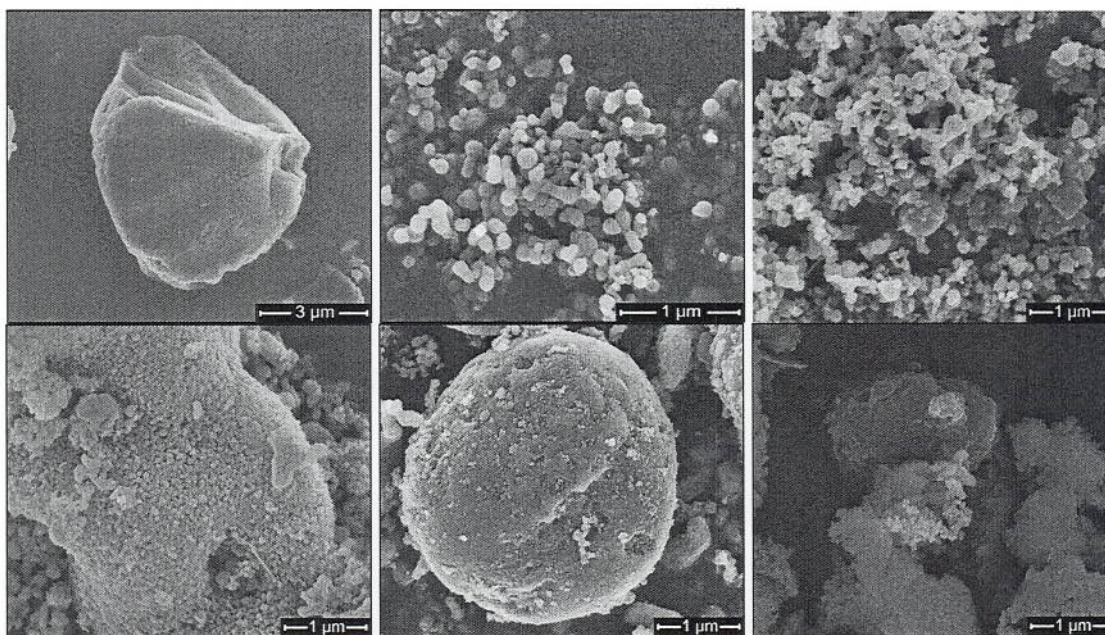


Figure 3. Typical SEM images for (1) Vesta PSi\_E3, (2) US Research Nanomaterials, (3) American Elements, (4) SACS#1, (5) SACS#2, and (6) SACS#3 nSi types.

Reactive mixtures composed of 44/51/5 wt.% Si/PTFE/FC-2175 SiTV was selected for this study as Yarrington *et al.* [13] observed that this fuel rich formulation yielded a faster burning than stoichiometric ratios. However, the calculated adiabatic temperature via the equilibrium code, Cheetah 6.0 [30] drops from 3443.6 K (stoichiometric: 20.8/74.2/5 SiTV) to 2836.7 K (44/51/5 wt.% SiTV). It should also be noted that all SiTV mixture ratios were held constant, and thus the oxygen content of each nSi type was not accounted for.

Reactive mixtures of SiTV were made by mixing nSi (see Table 1), PTFE (DuPont™ Zonyl® MP 1100) and FC-2175 (3M Fluorel™ Fluoroelastomer). FC-2175 is a 60/40 wt.% copolymer of Vinylidene Fluoride and Hexafluoropropylene and was used as the SiTV binding agent as it has been shown to increase ease of handling and reduce compact voids [13]. The binder is prepared by dissolving FC-2175 in acetone at a concentration of 1g FC-2175 per 20 ml acetone. 2g batches of SiTV were created by combining measured dry constituents (nSi and PTFE) with 2 ml of the FC-2175/acetone solution in an ESD safe container. The reactive mixture was then placed onto a Resodyn LabRam mixer preset with the following settings: 45% intensity for 1 minute, followed by 85% intensity for 4 minutes. Following the mixing process, the highly viscous mixture was spread into a dish and placed on a hotplate at 30 °C until the mixture was fully dried. The resulting powdered material was pressed to a stop into 6.35 mm diameter pellets at 78% percent theoretical maximum density (%TMD). Each pellet was then adhered to ¼-20 hex bolts, and vacuum grease (Dow Corning® High Vacuum Grease) was used to inhibit the radial sides.

#### SiTV VIS/IR Spectroscopy and Burn Rate Measurements

A burn plate with a 9.5 mm diameter through hole was mounted to an optics table. A spectrometer was also mounted to the optics table 50 cm from the sample location such that the imaging slit (0.5 mm x 5.0 mm) would be ~2.5 mm from the base of each pellet and normal to the direction of deflagration. A Spectraline VS100 Imaging Spectrometer sampling at 12 kHz was used to analyze the visual spectrum (VIS, 0.55 µm to 1.02 µm). A Spectraline ES100 Imaging Spectrometer sampling at 1.32 kHz was used to analyze the infrared spectrum (IR, 1.11 µm to 4.75 µm). A Cannon XL2 3CCD Digital Video Camcorder operating at 30 fps was also aligned with the pellet in order to visualize pellet deflagration and determine



propagation rates. A diagram of this experimental setup and alignment is illustrated in Figure 4. Each pellet was placed on the burn plate, and initiated with coiled 30 gauge Nichrome wire at 10V and  $18 \pm 3$  mg loose mechanically activated Ni/Al powder (planetary mill, 1:1 molar ratio, dry milled 15 minutes, wet milled in hexanes 15 minutes).

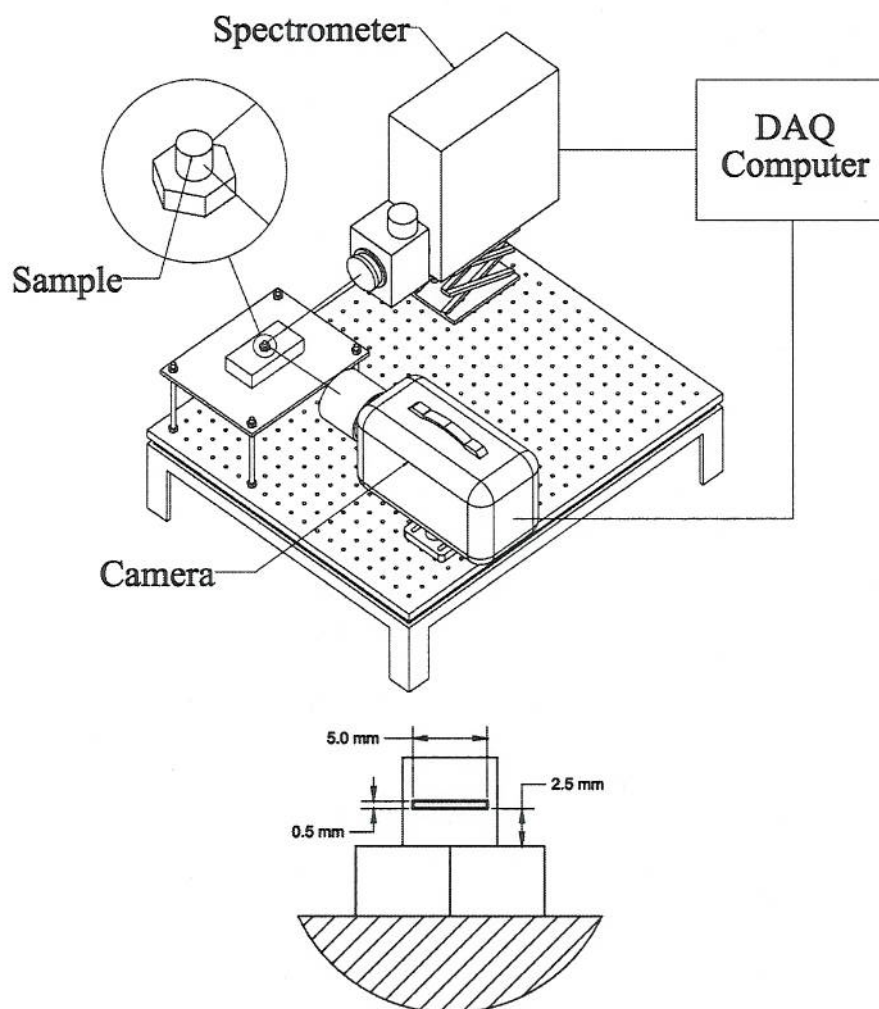


Figure 4. (Top) A diagram of the experimental setup used for SiTV combustion experiments. (Bottom) A diagram of the spectrometer alignment with a SiTV pellet.

Condensed phase carbon (i.e., soot) is theoretically a primary product species according to the general stoichiometric reaction for Si with PTFE:



This formation of soot as the dominant carbon-containing species is supported by the equilibrium code, Cheetah 6.0 [30], though it is also calculated that some excess silicon will react with carbon to form condensed phase SiC at fuel rich ratios (44/51/5 SiTV). Due to the large concentration of soot, it can be assumed that the SiTV combustion plume follows a grey body profile in the VIS-IR spectrums. Thus, the best fit grey body profile was superimposed on each VIS and IR spectral intensity profile in order to determine temperature and apparent emissivity of the combustion plume. This was accomplished through a coefficient of determination ( $R^2$ ) maximization algorithm using Planck's Law, which states that:



$$W_{\lambda} = \varepsilon \cdot \frac{2 \cdot \pi \cdot h \cdot c^2}{\lambda^5} \cdot \frac{1}{e^{\frac{h \cdot c}{\lambda \cdot T}} - 1} \quad (4)$$

where  $W_{\lambda}$  is spectral emittance of a grey body [ $W \cdot cm^{-2} \cdot \mu m^{-1}$ ],  $\varepsilon$  is emissivity [ $W_{\lambda}/W_{\lambda,black\ body}$ ],  $\lambda$  is wavelength [ $\mu m$ ],  $h$  is Planck's constant [ $6.6260755 \cdot 10^{-34} W \cdot s^2$ ],  $T$  is temperature [ $K$ ],  $c$  is the speed of light [ $2.99792458 \cdot 10^{10} cm \cdot s^{-1}$ ] and  $k$  is the Boltzmann constant [ $1.380658 \cdot 10^{-23} W \cdot s \cdot K^{-1}$ ]. By comparing VIS and IR spectral intensity profiles ( $I_{\lambda} = f(\lambda)$ ) with grey body profiles as calculated from Planck's Law ( $I_{\lambda} = f(\lambda, T, \varepsilon)$ ), a single temperature-emissivity combination can be found that will maximize the  $R^2$  value in respect to wavelength between the two intensity profiles. However, as a maximum  $R^2$  value can be found for any spectral intensity profile (e.g. curve-fitting background noise), a minimum  $R^2$  value of 0.95 was selected in order to abate erroneous temperature and emissivity measurements from altering reportable statistics.

## Nanoscale Silicon Results and Discussion

### SACS PSi Synthesis and nSi Powder Characterization

The synthesis of nSi by a reduction-type combustion method without the addition of any alkali metal halides has been reported by Yermekova et al. [27]. In this study, solid sodium chloride was added to the binary  $SiO_2/Mg$  exothermic reduction-type reaction to produce PSi. The SACS method has been reported in the past to investigate the combustion process in solid phase reactions with different inorganic salts of alkali metal halides (e.g. LiCl, NaCl, KCl) [28]. These alkali metal halides are typically utilized to control synthesis temperature and to preserve nanostructure of the as-synthesized products. When the salt fraction is high (i.e.,  $\alpha$  increases), the combustion temperature is correspondingly low. In this case, the molten salt forms a strong protective layer around the primary PSi particles, thus preserving their nanostructure. At a higher temperature (i.e., low salt concentration), the mobility of molten salt is high and the protective effect is not as strong, so particle size increases during combustion. In addition, lower salt concentration also increases the NaCl gas phase evolutions, as the boiling point of NaCl is 1686 K. This results in mass loss (due to NaCl gasification), incomplete reduction reaction (less Mg present), and further hinders preserving the PSi nanostructure.

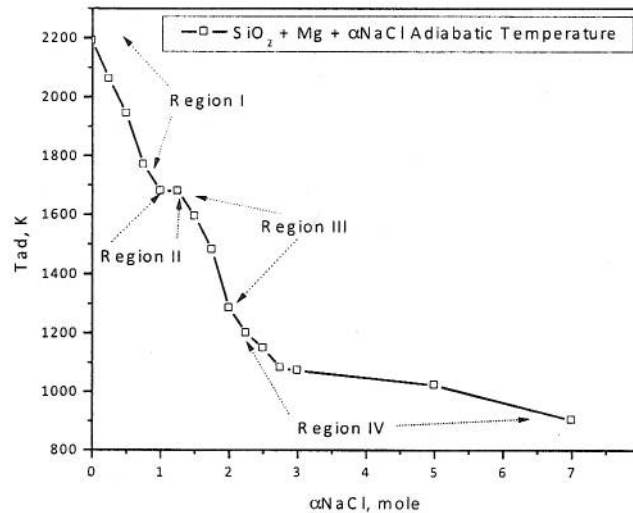


Figure 5.  $SiO_2/Mg$  adiabatic combustion temperature [ $K$ ] as a function of NaCl addition [mole].

The relationship of the adiabatic combustion temperature of  $SiO_2/Mg$  in the reactor as a function of NaCl addition (mole) was evaluated by the thermodynamic software "THERMO" [31] and the results are shown

in Figure 5. It should be outlined that the applied Ar pressure in the reactor (15–30 atm) hindered the amount of undesirable phases (i.e.,  $\text{MgSi}_2\text{O}_4$ ,  $\text{Mg}_2\text{Si}$ ,) and gas phases evolutions (Mg, NaCl), resulting in almost 99.999 % pure silicon [27]. Second, thermodynamic considerations suggested that without any salt addition the adiabatic combustion temperature of the  $\text{SiO}_2/\text{Mg}$  system would be close to 2200 K, which surpasses the melting points of Mg (922 K), Si (1687 K), and  $\text{SiO}_2$  (1923 K) as well as the boiling point of Mg (1363 K). It can be seen that the adiabatic combustion temperature showed a linear decrease in Region I ( $0 \leq \alpha \leq 1$ ) and reached a plateau in Region II ( $1 \leq \alpha \leq 1.25$ ), followed by a further decrease to the stoichiometric point (Region III,  $1.25 \leq \alpha \leq 2$ ) and a non-linear decrease in Region IV ( $\alpha > 2$ ). As any exposure to temperatures in excess of 1687 K (m.p. of Si) may sinter the as-synthesized silicon microstructures, selecting the appropriate  $\alpha$  values ( $1 \leq \alpha \leq 2$ ) will avoid melting/coarsening of as-synthesized PSi. Therefore it was reasonable to choose  $1 \leq \alpha \leq 2$  as the experimental parameters, which correspond to combustion temperatures ranging from 1284 K to 1680 K. In practice, all the measured combustion temperatures were lower than the calculated values [31]. In short, this phenomenon can be explained by the heat losses from reactants to the graphite crucible and to the surrounding gas phase during the experiments, which led to lower combustion temperatures than the thermodynamically predicted ones. Experimental parameters such as sample geometry, crucible size, and Ar chamber pressure can also have significant influences on the combustion process.

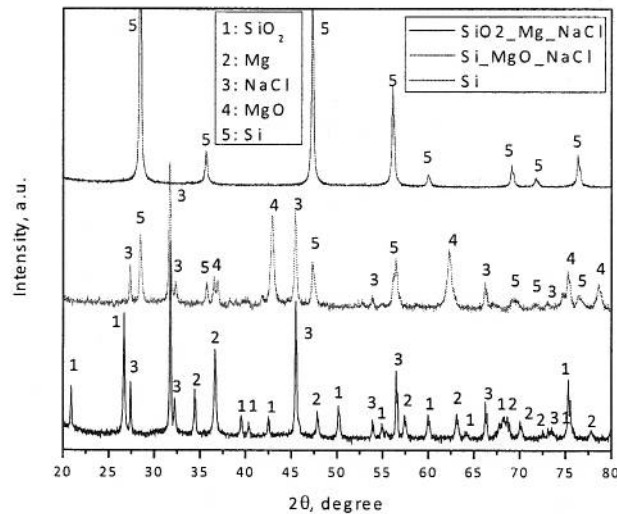


Figure 6. Typical XRD patterns of initial reactants, as-synthesized products, and post-treatment PSi.

After synthesis and cooling down in the reactor, the as-synthesized product was collected for further hydrometallurgical treatments. It should be noted that the as-synthesized PSi/MgO/ $\alpha$ NaCl product was partially sintered due to a short-term exposure to high temperatures during the reaction. Therefore, a mortar and pestle was used to slightly grind the product into a powder form. Typical XRD patterns of initial reactants, as-synthesized products, and as-leached PSN were shown in Figure 6. As can be seen in Figure 6a, three phases were identified (i.e.,  $\text{SiO}_2$ , Mg, and NaCl). Figure 6b showed the as-synthesized products (PSi, MgO, and NaCl). After the HCl hydrometallurgical treatment and filtering was used to leach out MgO and NaCl, only the crystalline PSi can be seen (Figure 6c). Note that all the as-leached PSi powders were further characterized by EDS measurements to determine the residual of other elements (e.g. Mg, Na, Cl, etc).



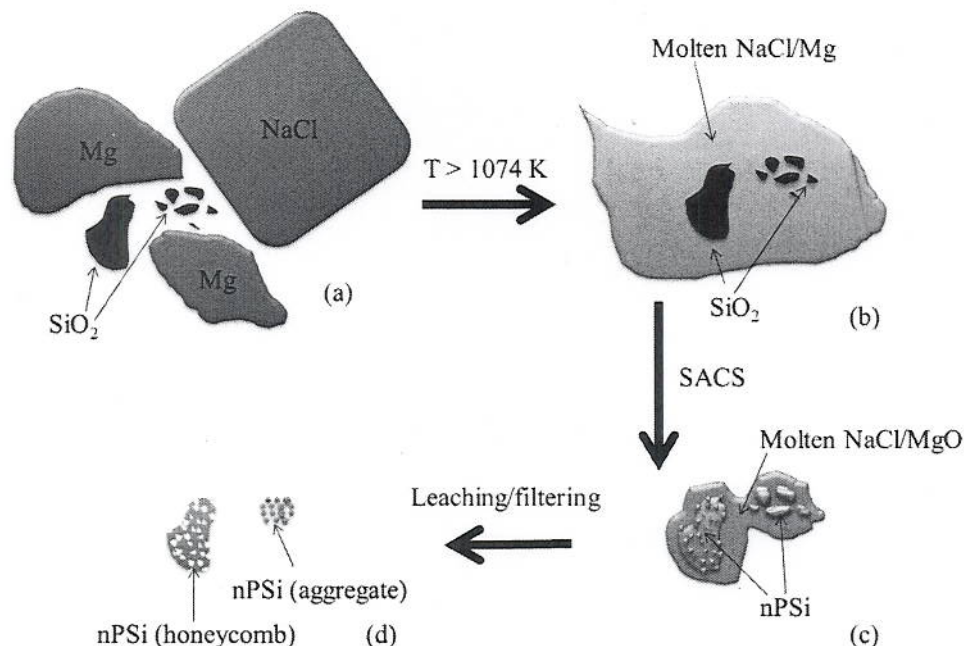


Figure 7. Proposed mechanisms of SACS in the  $\text{SiO}_2/\text{Mg}/\text{NaCl}$  system.

A proposed PSi mechanism of SACS in the investigated  $\text{SiO}_2/\text{Mg}/\text{NaCl}$  system is illustrated in Figure 7. In Figure 7a the initial reactants ( $\text{SiO}_2$ ,  $\text{Mg}$ ,  $\text{NaCl}$ ) were shown, followed by the melting of  $\text{Mg}$  and  $\text{NaCl}$  (Figure 7b) when the temperature reached  $>1074 \text{ K}$  (m.p. of  $\text{NaCl}$ ). The molten  $\text{Mg}/\text{NaCl}$  phase covered  $\text{SiO}_2$  non-uniformly. The SACS reaction was then triggered afterwards (Figure 7c), converting the initial reactants to the final products (PSi,  $\text{MgO}$ ,  $\text{NaCl}$ ). Note that the main reason for two different final PSi morphologies was due to the broad size distribution of the  $\text{SiO}_2$  initial precursor (i.e., sub-micron to several microns). Hydrometallurgical treatment of the combustion product was carried out with different acids ( $\text{HCl}$ ,  $\text{HF}$ ,  $\text{HNO}_3$ ) to obtain PSi (Figure 7d) with the two different morphologies (i.e., honeycomb and small particle aggregates and agglomerates). Again, it should be addressed that with the applied Ar pressure the gas phase evolutions of  $\text{Mg}_{(\text{g})}$  and  $\text{NaCl}_{(\text{g})}$  were minimized. Therefore, there was almost no loss of initial reactants during the reaction and the yield ( $\sim 20 \%$ ) was very close to estimated values.



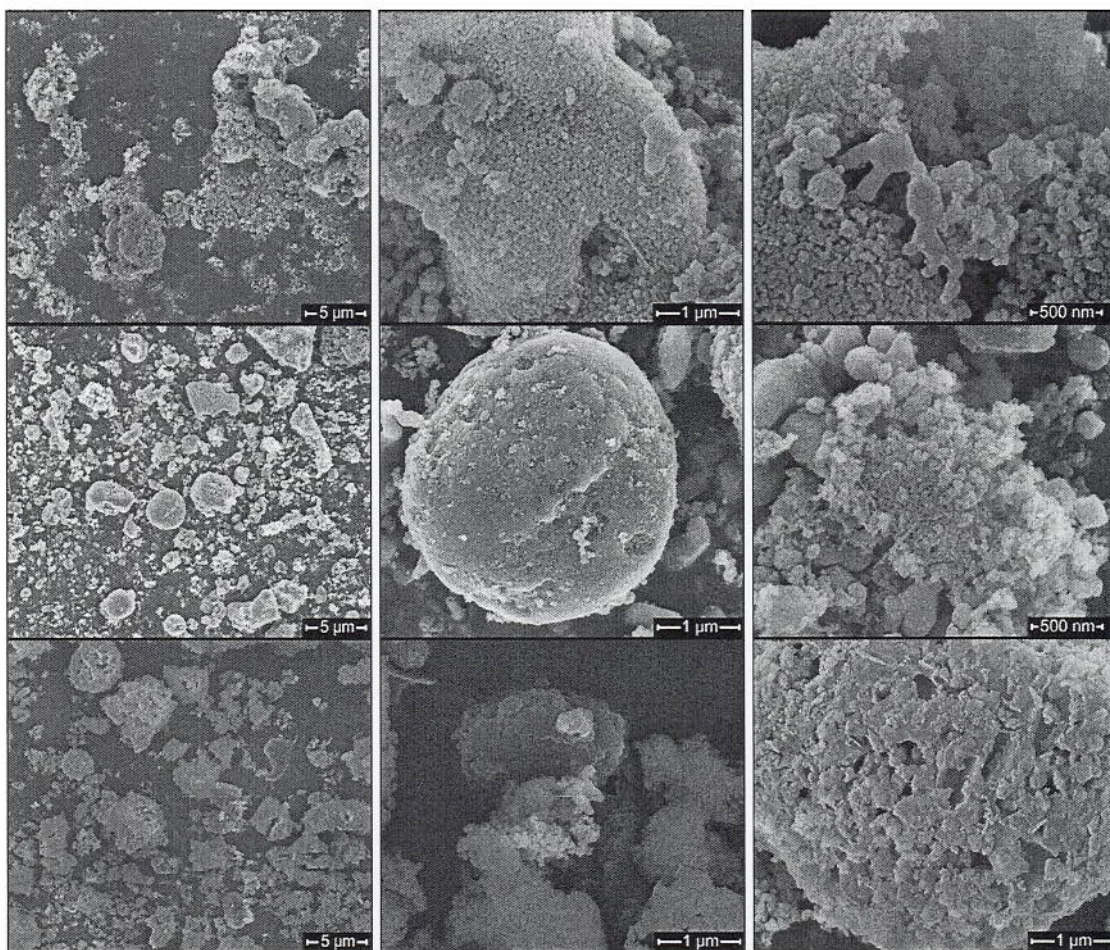


Figure 8. Typical SEM images of as-leached SACS#1 (A-C), SACS#2 (D-F), and SACS#3 (G-I).

By varying  $\alpha$  in the SACS mechanism, it was observed from the microstructural observation standpoint that a higher NaCl concentration did not show many differences in terms of morphology and size. However, with a higher  $\alpha$  value the PSi yield ( $\gamma$ ) decreased from 20 % to 10 %, which was less preferable for scaled-up systems. Therefore, a constant  $\alpha=1$  was employed for all SACS samples used in combustion experiments. It was, however, observed that the key parameter for producing different PSi powders was the hydrometallurgical treatments. Three sets of PSi were produced and abbreviated as SACS#1 (5% HCl concentration), SACS#2 (5% HCl concentration with additional multi-acid treatments), and SACS#3 (30% HCl concentration). Typical SEM images of SACS#1-3 are shown in Figure 8. It can be seen from Figure 1 that the initial  $\text{SiO}_2$  and  $\text{MgO}$  powders had particle size distributions of 0.2-5  $\mu\text{m}$  and 5-50  $\mu\text{m}$  respectively, while NaCl particles were  $\sim 300 \mu\text{m}$  in size. The as-leached SACS#1 and SACS#3 primarily consisted of highly porous aggregates and honeycomb like particles. At higher magnification of SACS#1 and SACS#2 particles, it is clear that the larger particles were fully covered with aggregates comprised of  $\sim 50 \text{ nm}$  particles and 10-20 nm particles respectively. The outer aggregates in SACS#3 appeared almost fluffy in morphology, which caused the high SSA reported in Table 1. SACS#2, however, showed little resemblance to SACS#1, even though an equivalent HCl concentration was used. As shown in Figure 8 (D-E), it is clear that the high SSA surface features surrounding the larger particles were almost entirely removed following the additional multi-acid hydrometallurgical treatment. However, as shown in Figure 8F it can be seen that at least some of the high SSA surface features do survive the additional hydrometallurgical treatment, which most likely contributed to a majority of the SSA reported in Table 1. As SACS#2 has 90% less oxygen content than SACS#1, it can thus be hypothesized that a majority of the

oxygen content is in the high SSA surface features rather than in the larger particle cores. This would suggest that the high oxygen content found in SACS#3 is also a result of the high SSA aggregates found surrounding the larger particles.

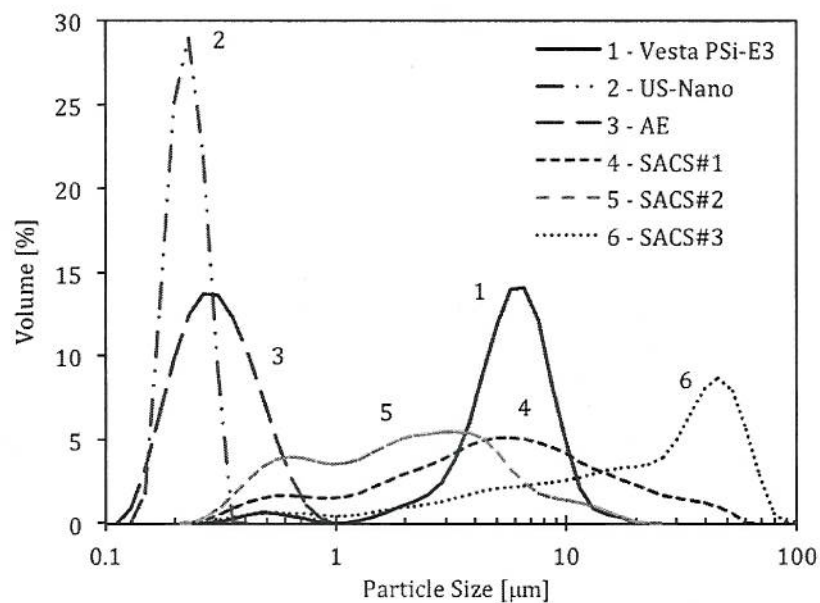


Figure 9. The mean particle size of each nSi type.



Table 2. Mean Particle Size [ $\mu\text{m}$ ].

nSi Number	Silicon Type	D <sub>50</sub> Arithmetic	D <sub>4,3</sub> Volume Weighted	D <sub>3,2</sub> Surface Weighted
1	Vesta PSi_E3	5.41	5.57	3.64
2	US Research Nanomaterials	0.21	0.23	0.22
3	American Elements	0.27	0.32	0.28
4	SACS #1	4.67	7.71	2.16
5	SACS #2	1.92	2.77	1.19
6	SACS #3	23.61	27.52	5.38

It is shown in Figure 9 that SACS#1-3 powders have very wide particle distributions which are characterized by both large and small Si particles. In order to allow equal biasing of both the large and small particle sizes, the D<sub>3,4</sub> and D<sub>3,2</sub> mean particle sizes are presented in Table 2 respectively. It should be noted that while SACS#1-2 have slightly bimodal distributions, their volume and surface weighted means are still relatively close. SACS#3, however, has a very wide particle size distribution with a dominant peak at  $\sim 30 \mu\text{m}$ , resulting in a significant difference between the volume and surface weighted means. In contrast, Vesta PSi\_E3 nSi powder was found to have a narrow distribution with a mean particle size of  $\sim 5 \mu\text{m}$ . US-Nano nSi powder is comprised of small, spherical nanoparticles, as confirmed by SEM imaging.

In summary, the SACS process was used to reduce the combustion temperature of the SiO<sub>2</sub>/Mg SHS reaction through the use of NaCl. An optimum amount of NaCl was calculated through thermodynamic analysis to be ( $1 \leq \alpha \leq 2$ ) in order to be stay below the m.p. of silicon while still maintaining an acceptable PSi yield. It was determined that an increased HCl concentration in the hydrometallurgical leaching treatment will increase the SSA, oxygen content and dominant particle size of the resulting powder. Three nSi powders using different hydrometallurgical treatments (SACS#1-3) were synthesized via SACS in order to undergo combustion experiments designed to determine the dominant powder characteristics driving Si/PTFE reactions.

#### SiTV Combustion Characteristics

In order to systematically examine material characteristics, such as specific surface area, morphology, oxygen content (active content), and dominant particle size, three commercial nSi powders and the three SAC powders were used. As many of these nSi types (all but US-Nano and AE) are nano-featured, but micron in dominant particle size (see Figure 9 and Table 2), it can then be assumed that initial ignition of each nSi particle simply reacts the highly reactive outer surface features (high SSA) with the PTFE decomposition products, essentially leaving the effective core (low SSA) to slowly regress as the particle reacts with the highly reactive gas phase fluorine compounds and entrained ambient oxygen. By assuming that the volume weighted mean particle size (D<sub>4,3</sub>) is proportional to the effective particle core size for each nSi type, it can be seen by comparing Figure 13 with Table 2 that as the particle core size decreases, the average burning rate increases. It is known from the shrinking core model [32] that as a particle's core size decreases, the time it takes to completely react each particle also decreases. This relationship between burning rate and dominant particle core size is shown in Figure 11.



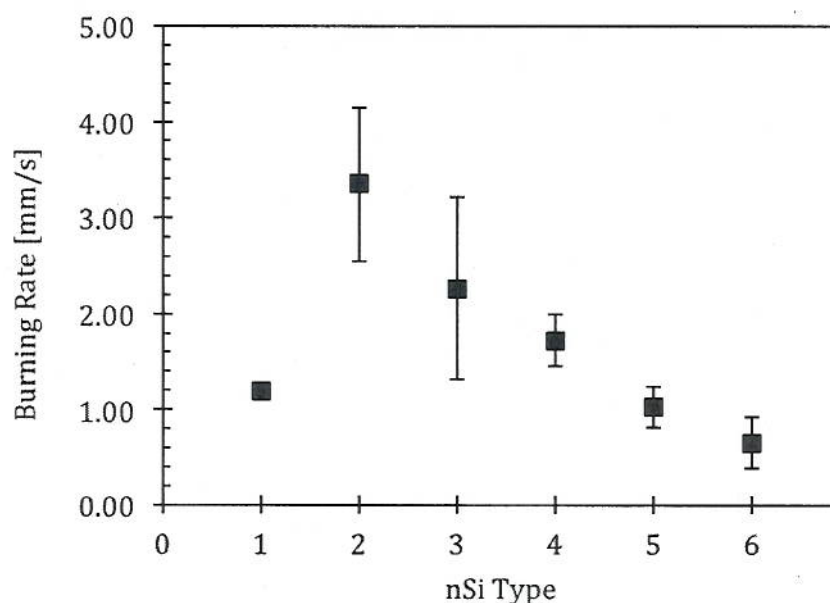


Figure 10. Measured burning rate for each nSi type. All data points were taken with a repeat of 5. It should be noted that the error bar for Vesta PSi\_E3 (nSi type 1) is too small to be visible with at the current burning rate scale.

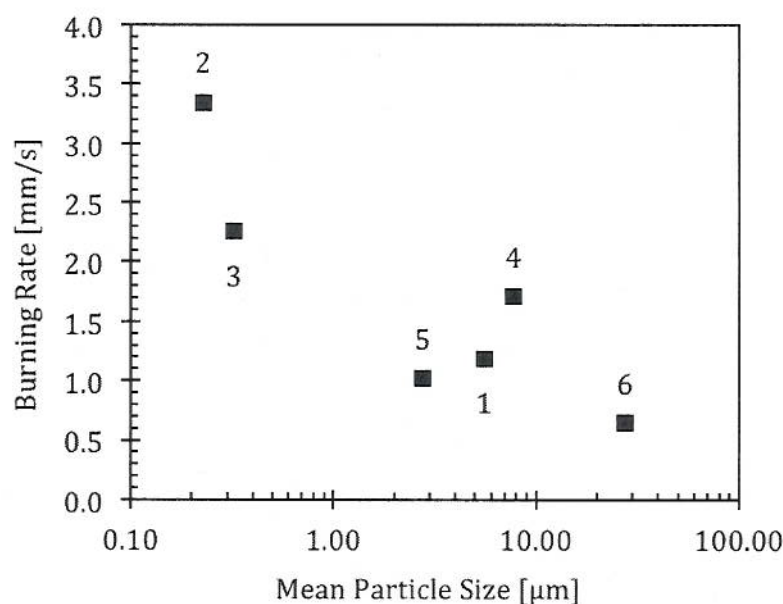


Figure 11. A plot of burning rate as a function of dominant particle size (volume weighted mean particle size,  $D[4,3]$ ).

As shown in Figure 11 US-Nano and AE burning rates were higher than any other nSi types compared in this study. These particular nSi powders are comprised of small, spherical particles with a small mean particle size. Thus, there is a significantly smaller effective core, which results in a faster burning rate. This same trend is observed with the other nSi types, which are high SSA, micron sized powders. SACS#3, which has the largest mean particle size, also has the slowest regression rate. Vesta PSi-E3 and

SACS#1 and SACS#2 all have burning rates within 0.7 mm/s (~40%) of each other, but not necessarily in order of receding mean particle size. Vesta PSi-E3 and SACS#1-2 are nano-porous in morphology, though the pore depth and percentage of each particle that is porous/nano-featured is unknown. For example, it can be seen in Figure 12 that the pores in SACS#1 do not necessarily encompass the full outer geometry of every Si particle. Therefore, it cannot be assumed that the entire internal geometry of a nano-porous particle is in fact porous, suggesting that the burning rate order observed in Figure 11 is in fact representative of the effective core sizes. Thus, it appears that the dominant parameter influencing SiTV burning rate is the dominant particle size. This trend was also observed for nSi/NaClO<sub>4</sub> burning rates published by Thiruvengadathan *et al.* [10] indicating that nSi particle geometries greatly influenced burning rates (lower aspect ratios increase burning rates).

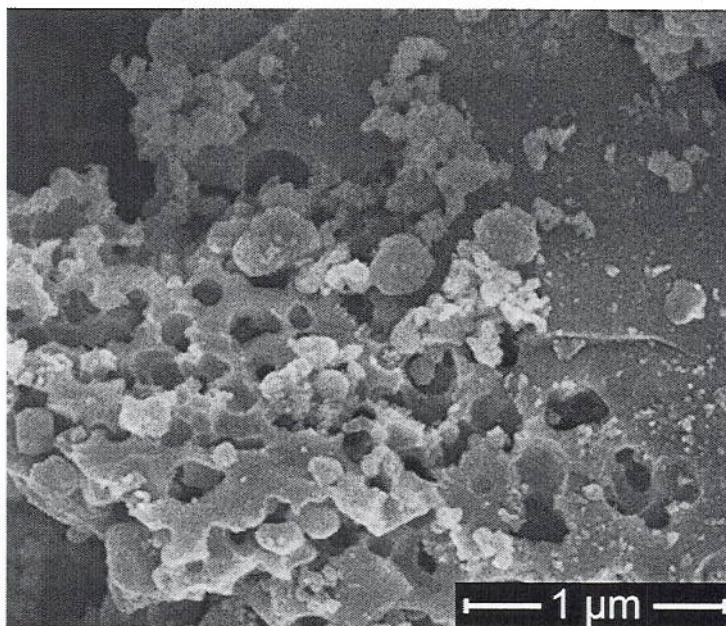


Figure 12. SEM of SACS#1 PSi at 40k magnification depicting a single Si particle that is not fully porous on its outer surface.

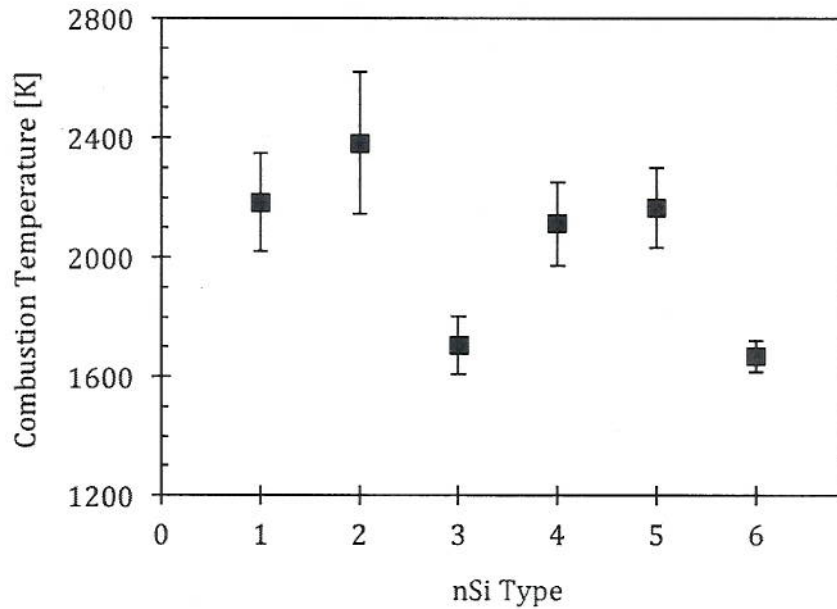


Figure 13. Measured combustion temperature for each nSi type. All data points were taken with a repeat of 5.

This trend was not evident with combustion temperature measurements (Figure 10), which is driven by nSi powder oxygen content. It can be seen by comparing Figure 13 with Table 1 that combustion temperature appears to drop significantly with increased oxygen content. From Table 1, it is shown that AE powder has the highest measured oxygen content of ~22 wt.%  $O_2$ , which indicates that AE nSi powder is comprised of roughly 83%  $SiO_2$ . Accounting for the high oxygen content in thermal equilibrium calculations via Cheetah 6.0 [30], results in a predicted combustion temperature drop from 2836.7 K to 1742.7 K. Likewise, SACS#3 powder (14-15 wt.%  $O_2 \rightarrow 52-56\%$   $SiO_2$ ) also yields a drop in predicted combustion temperature to 1899.6 K. Figure 14 shows the predicted combustion temperature of the 44/51/5 wt.% SiTV composition as a function of active nSi powder. The measured combustion temperatures previously shown in Figure 13 are also plotted with the predicted combustion temperatures. This shows that the measured flame temperature does appear to generally follow the predicted flame temperatures, indicating that the nSi powder oxygen content plays a significant role in limiting SiTV combustion temperatures. Thus, it is concluded that oxygen content is the primary characteristic driving combustion temperature of Si/PTFE.



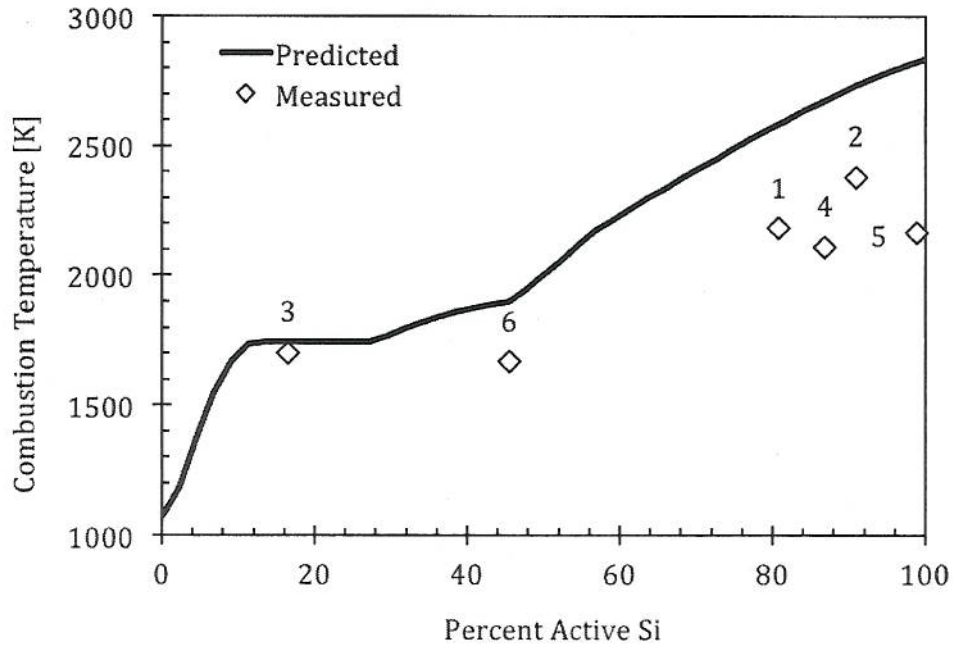


Figure 14. Predicted and measured combustion temperature as a function of percent active silicon.

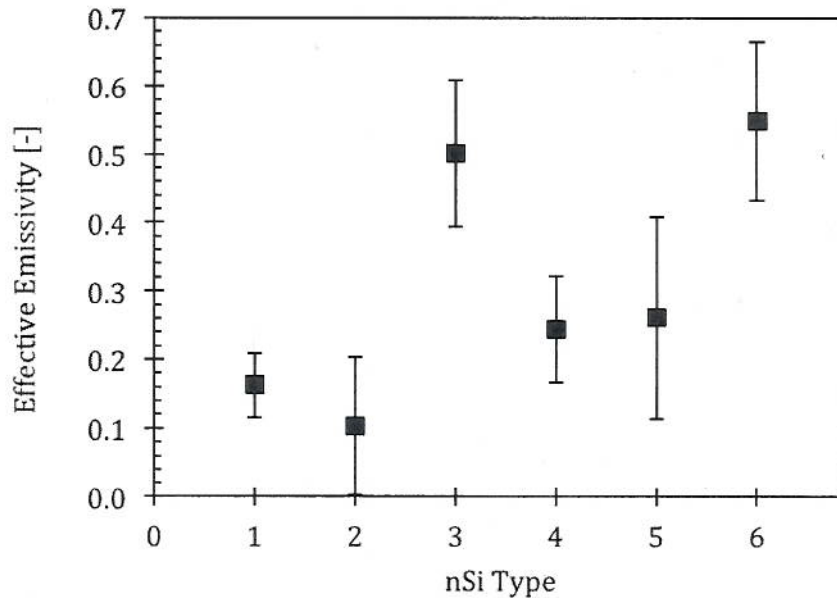


Figure 15. Measured effective plume emissivity for each nSi type. All data points were taken with a repeat of 5.

This trend was also evident for effective plume emissivity measurements (Figure 15). Effective plume emissivity appears to have an inverse relationship with combustion temperature, which is congruent with the oxidation of soot particles [33]. Soot has been shown to begin oxidizing in air at  $\sim 1800$  K as well as be temperature dependent in its oxidation rate. It can be assumed that a significant amount of air is entrained in the plume during combustion, thus at temperatures exceeding 1800 K the excess soot begins

to oxidize into CO<sub>2</sub>. As US-Nano had an average flame temperature of 2348 K, it is not surprising that it had an average effective emissivity of only 0.09. Conversely, SACS#3 had an average flame temperature of only 1667 K and an effective emissivity of 0.55, suggesting that there was a much higher soot concentration within the combustion plume. Another factor that may have increased emissivity is the predicted presence of liquid SiO<sub>2</sub> in the combustion products with wt.% SiO<sub>2</sub> greater than ~50% in the nSi powder. We expect that liquid SiO<sub>2</sub> aides in the formation of monoliths comprised of carbon soot and other various condensed phase product species. For example, monolith formation was observed for American Elements and SACS#3 based SiTV reactive mixtures (high oxygen content, reduced combustion temperature).

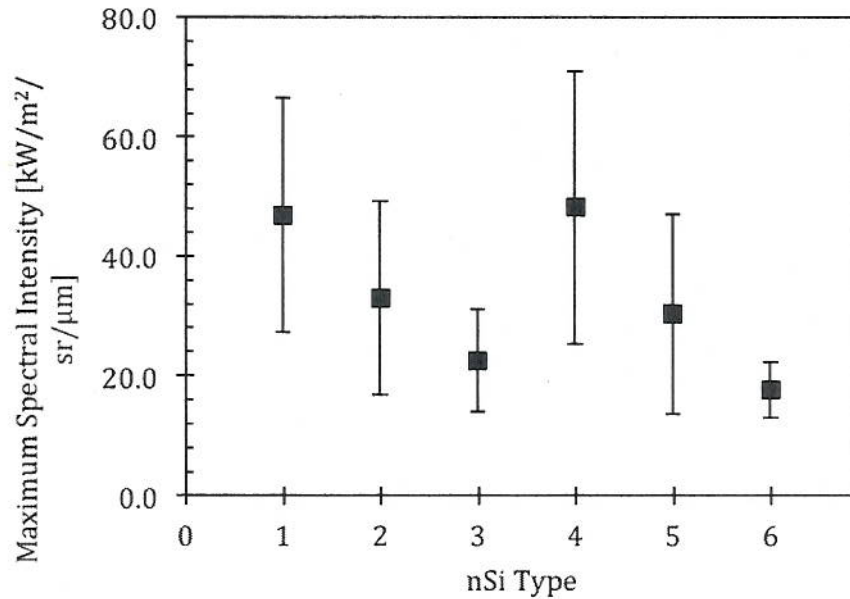


Figure 16. Measured maximum Spectral Intensity for each nSi type. All data points were taken with a repeat of 5.

Spectral intensity, however, appears to be driven by both temperature and emissivity. As previously discussed, as measured temperature increased, effective plume emissivity decreased. From equation

$$W_{\lambda} = \epsilon \cdot \frac{2 \cdot \pi \cdot h \cdot c^2}{\lambda^5} \cdot \frac{1}{e^{\frac{h \cdot c}{\lambda \cdot T}} - 1}$$

(4) it can be seen that an increase in

temperature will increase intensity while a decrease in emissivity will lower intensity. Thus, there must be a point at which the drop in emissivity will overpower the rise in temperature. As shown in Figure 16, Vesta PSi-E3 and SACS#1 produced the highest SiTV maximum spectral intensities. These two SiTV reactive mixtures had an average combustion temperature of ~2146 K and an average effective emissivity of ~0.20. This may suggest that temperatures around ~2150 K may produce the maximum SiTV intensity before the drop in emissivity begins to overpower the increase in temperature. However, equation (4) can be used to predict the maximum spectral intensity as a function of combustion temperature and effective emissivity. By plotting effective plume emissivity as a function of combustion temperature (see Figure 17), it can be seen that the decrease in effective emissivity is fairly linear. By assuming that this linear regression in emissivity is in fact representative of the system, equation (4) can be used to predict the maximum spectral intensity knowing that Wien's displacement law states that peak wavelength of a black body curve is given by,



$$\lambda_{\max} = \frac{b}{T}, \quad (5)$$

where  $b$  is a constant ( $b = 2.8977685 \cdot 10^{-3} \text{ m} \cdot \text{K}$ ). Figure 17 shows the predicted maximum spectral intensity as function of combustion temperature and effective emissivity along with the measured maximum spectral intensity for each nSi type. All nSi types generally follow the predicted maximum spectral intensity with the exception of SACS#2 (powder #5), which has a measured spectral intensity that is much lower than the predicted value. It can also be seen from the predicted maximum spectral intensity profile that a maximum spectral intensity should be at a temperature of  $\sim 2100 \text{ K}$ , which corresponds to original observations and experimental results.

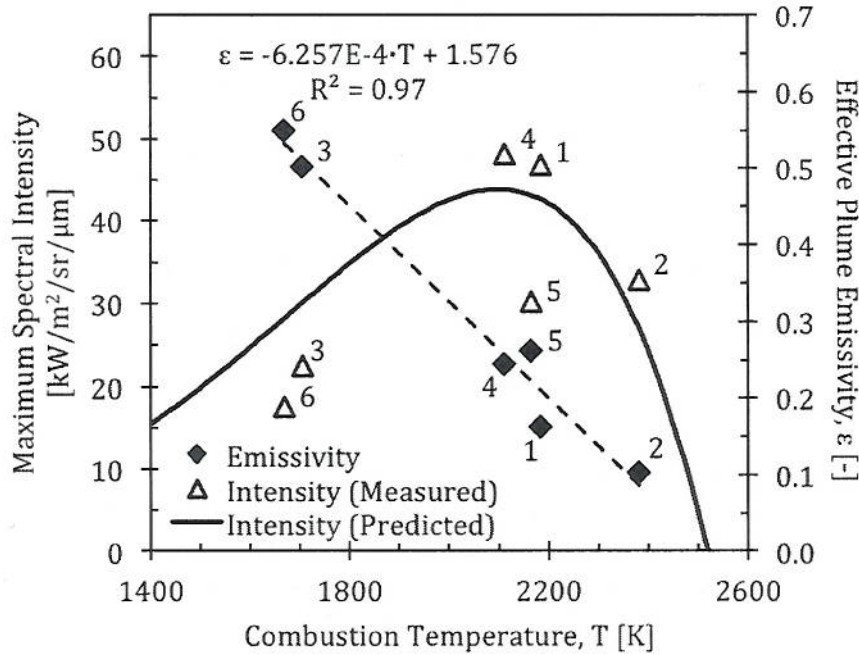


Figure 17. Maximum spectral intensity (predicted and measured) as a function of combustion temperature and effective plume emissivity. The dashed line corresponds to a linear fit of emissivity as a function of combustion temperature that is used in predicting the maximum spectral intensity from equation (4).

### Summary/Conclusions of Nanosilicon Efforts

Salt assisted combustion synthesis was used to produce tailored PSi powder with varied SSA and oxygen content. The SACS combustion process was characterized for optimum salt addition, and the influence of acid concentration in the hydrometallurgical process was discussed. Three SACS nSi powders were synthesized and combustion experiments were utilized to compare the synthesized powders to three commercial nSi powders (Vesta PSi-E3, US-Nano, and AE). Each powder was mixed into a specific SiTV formulation, burned at ambient conditions, and compared in respect to combustion temperature, burning rate, maximum spectral intensity, and apparent plume emissivity. In summary, it was observed that Si/PTFE combustion is greatly influenced by nSi powder characteristics. It was shown that burning rate of the nSi/PTFE system is highly dependent on dominant particle size. As expected the measured combustion temperature was limited by the oxygen content in the nSi powder, which in turn was the driving parameter for effective plume emissivity and spectral intensity. As intensity is a function of effective plume emissivity and temperature, it was proposed that a combustion temperature of  $\sim 2100 \text{ K}$

may maximize intensity without a significant decrease in effective emissivity as a result of oxidizing soot with entrained air. No quantitative statement could be made from the data as to the influence of SSA on Si/PTFE combustion, though it may have a significant role in SiTV ignition. The exception to this observation was SACS#3, which was more difficult to ignite, most likely due to the excess oxygen content in the nSi powder. Therefore, it is concluded that the driving parameters for the combustion of the Si/PTFE are dominant particle core size and oxygen content.

## Nanosilicon References

1. Koch, E.-C. and D. Clément, *Special Materials in Pyrotechnics: VI. Silicon – An Old Fuel with New Perspectives*. Propellants, Explosives, Pyrotechnics, 2007. **32**(3): p. 205-212.
2. Ellern, H., *Military and civilian pyrotechnics*. 1968, New York,: Chemical Pub. Co. xii, 464 p.
3. Hale, G.C., *Delay powder*, 1931: United States.
4. Rugunanan, R.A. and M.E. Brown, *Combustion of Binary and Ternary Silicon Oxidant Pyrotechnic Systems .2. Binary-Systems with Sb<sub>2</sub>O<sub>3</sub> and KNO<sub>3</sub> as Oxidants*. Combustion Science and Technology, 1994. **95**(1-6): p. 85-99.
5. Rugunanan, R.A. and M.E. Brown, *Combustion of Binary and Ternary Silicon Oxidant Pyrotechnic Systems .3. Ternary-Systems*. Combustion Science and Technology, 1994. **95**(1-6): p. 101-115.
6. Rugunanan, R.A. and M.E. Brown, *Combustion of Binary and Ternary Silicon Oxidant Pyrotechnic Systems .1. Binary-Systems with Fe<sub>2</sub>O<sub>3</sub> and SnO<sub>2</sub> as Oxidants*. Combustion Science and Technology, 1994. **95**(1-6): p. 61-83.
7. Rugunanan, R.A. and M.E. Brown, *Combustion of Binary and Ternary Silicon Oxidant Pyrotechnic Systems .4. Kinetic Aspects*. Combustion Science and Technology, 1994. **95**(1-6): p. 117-138.
8. Rugunanan, R.A. and M.E. Brown, *Reactions of powdered silicon with some pyrotechnic oxidants*. Journal of Thermal Analysis and Calorimetry, 1991. **37**(6): p. 1193-1211.
9. Krishnamohan, G., E.M. Kurian, and H.R. Rao, *Thermal Analysis and Inverse Burning Rate Studies on Silicon-Potassium Nitrate System*, in *8th International Pyrotechnics Seminar* 1982: Steamboat Springs, CO. p. 404.
10. Thiruvengadathan, R., et al., *Combustion Characteristics of Silicon-Based Nanoenergetic Formulations with Reduced Electrostatic Discharge Sensitivity*. Propellants, Explosives, Pyrotechnics, 2012. **37**(3): p. 359-372.
11. Mason, B.A., et al., *Combustion performance of several nanosilicon-based nanoenergetic composites*. 2012.
12. Subramanian, S., et al., *Nanoporous Silicon Based Energetic Materials*, in *The 26th Army Science Conference: Transformational Army Science and Technology (S&T) - Harnessing Disruptive S&T for the Soldier* 2008: Orlando, FL.
13. Yarrington, C.D., S.F. Son, and T.J. Foley, *Combustion of Silicon/Teflon/Viton and Aluminum/Teflon/Viton Energetic Composites*. Journal of Propulsion and Power, 2010. **26**(4): p. 734-743.
14. Yetter, R.A., G.A. Risha, and S.F. Son, *Metal particle combustion and nanotechnology*. Proceedings of the Combustion Institute, 2009. **32**(2): p. 1819-1838.
15. Dreizin, E.L., *Metal-based reactive nanomaterials*. Progress in Energy and Combustion Science, 2009. **35**(2): p. 141-167.
16. Wei, D.G., R. Dave, and R. Pfeffer, *Mixing and characterization of nanosized powders: An assessment of different techniques*. Journal of Nanoparticle Research, 2002. **4**(1-2): p. 21-41.
17. Morita, M., et al., *Growth of native oxide on a silicon surface*. Journal of Applied Physics, 1990. **68**(3): p. 1272.
18. Wayner, D.D.M. and R.A. Wolkow, *Organic modification of hydrogen terminated silicon surfaces*. Journal of the Chemical Society-Perkin Transactions 2, 2002(1): p. 23-34.
19. Kovalev, D., et al., *Strong Explosive Interaction of Hydrogenated Porous Silicon with Oxygen at Cryogenic Temperatures*. Physical Review Letters, 2001. **87**(6).
20. Clément, D., et al., *Highly explosive nanosilicon-based composite materials*. physica status solidi (a), 2005. **202**(8): p. 1357-1364.



21. Churaman, W., L. Currano, and C. Becker, *Initiation and reaction tuning of nanoporous energetic silicon*. Journal of Physics and Chemistry of Solids, 2010. **71**(2): p. 69-74.
22. Książczak, A., H. Boniuk, and S. Cudziło, *Thermal decomposition of PTFE in the presence of silicon, calcium silicide, ferrosilicon and iron*. Journal of Thermal Analysis and Calorimetry, 2003. **74**(2): p. 569-574.
23. Panas, A.J., S. Cudziło, and J. Terpilowski, *Investigation of the thermophysical properties of metal - polytetrafluoroethylene pyrotechnic compositions*. High Temperatures-High Pressures, 2002. **34**(6): p. 691-698.
24. Bao, Z.H., et al., *Chemical reduction of three-dimensional silica micro-assemblies into microporous silicon replicas*. Nature, 2007. **446**(7132): p. 172-175.
25. Wynnyckyj, J.R. and D.B. Rao, *Mechanism of Reduction of Silica by Magnesium Vapor*. High Temperature Science, 1976. **8**(3): p. 203-217.
26. Banerjee, H.D., S. Sen, and H.N. Acharya, *Investigations on the Production of Silicon from Rice Husks by the Magnesium Method*. Materials Science and Engineering, 1982. **52**(2): p. 173-179.
27. Yermekova, Z., Z. Mansurov, and A.S. Mukasyan, *Combustion synthesis of silicon nanopowders*. International Journal of Self-Propagating High-Temperature Synthesis, 2010. **19**(2): p. 94-101.
28. Won, C.W., et al., *Refractory metal nanopowders: Synthesis and characterization*. Current Opinion in Solid State & Materials Science, 2010. **14**(3-4): p. 53-68.
29. Farrell, D., S. Limaye, and S. Subramanian, *Silicon Nanosponge Particles*, 2006: United States.
30. Bastea, S., et al., *Cheetah 6.0*, 2010: Lawrence Livermore National Laboratory.
31. Shiryayev, A.A., *Thermodynamics of SHS processes: An advanced approach*. International Journal of Self-Propagating High-Temperature Synthesis, 1995. **4**: p. 351-362.
32. Ishida, M. and C.Y. Wen, *Comparison of kinetic and diffusional models for solid-gas reactions*. AIChE Journal, 1968. **14**(2): p. 311-317.
33. Zhao, B., et al., *Particle size distribution function of incipient soot in laminar premixed ethylene flames: effect of flame temperature*. Proceedings of the Combustion Institute, 2005. **30**(1): p. 1441-1448.

## Doped Silicon

In the last period we have finalized our efforts examining the effect of doped silicon. This work is reported in a journal paper and appears in the Appendix.

## Multiscale Nanoporous Silicon Combustion

### Introduction for nanoporous silicon effort

While reactive wave propagation in porous silicon (PS)-oxidizer composites had been previously studied, the previous work has been limited to etching PS on low doped P-type substrates and testing it as is, with very little control over the reactive wave propagation. The work described here is a systematic examination of the various parameters that affect the reactive wave propagation, namely the composite equivalence ratio, oxidizer, nanoscale and microscale structure, and the effect of dopant atoms, followed by a demonstration of how the reactive composites can be engineered to achieve required energy release profiles. The effect of the substrate properties on PS composites was studied using both P and N-doped substrates with a wide range of dopant concentrations. A parametric study of the effect of mixture composition was carried out by quantifying the oxidizer deposition within nanometer scale pores and varying the oxidizer deposition to create composites with equivalence ratios ranging from unity to the fuel rich extinction limit. This revealed an equivalence ratio independent reactive wave propagation with very wide flammability limits, as predicted by the thermodynamic equilibrium calculations. While the reactive wave propagation speeds observed on heavily doped substrates were always low, between 1-10 m/s, low



doped substrates consistently exhibited high propagation speeds of several hundreds of m/s. This was attributed to the formation of a random micro-crack pattern on the low doped substrates resulting in the transition from a conductive burning regime to a convective burning regime. This hypothesis was validated by creating organized microscale structures on heavily doped substrates that consistently exhibited low speed propagations. These samples with organized microscale structures demonstrated reactive wave propagations of several hundreds of m/s similar to the low doped substrates. The various factors such as the permeability, pitch, and size of the microscale structure were studied to better understand the convective propagation mode and tune the reactive wave propagation speeds.

### **Experimental methods of nanoporous silicon effort**

The PS used in this work was prepared by electrochemical dissolution of silicon using electrolytes consisting of equal volumes of hydrofluoric acid and ethanol. The etch process was carried out in a Teflon etch cell capable of holding 250 ml of electrolyte and exposing only the top side of 4" silicon wafers to the electrolyte. During the etch process the silicon wafer acts as the anode, and a silver mesh, placed at a fixed distance from the surface of the wafer acts as the cathode. Electrical contact was established with the low doped P-type wafers (10 – 20  $\Omega$ -cm, Boron doped) by depositing a 20 nm thick layer of titanium on the backside of the wafer followed by a rapid thermal anneal at 700 °C in an Argon environment. The low doped N-type wafers (2 – 5  $\Omega$ -cm, Phosphorus doped) were etched under illumination. Uniform porous layers could be etched on the heavily doped wafers (0.001 – 0.005  $\Omega$ -cm, Boron or Arsenic doped) without the need of illumination or backside titanium deposition. Thick and stable porous layers were etched on the substrates using an etch-stop-etch method with several minute relaxation times between etch cycles. The etched wafers were cut into test samples 5 mm wide, which were used to study the reactive wave propagation. The porosity was estimated gravimetrically, by dissolving the porous films in a 1M aqueous sodium hydroxide (NaOH) solutions. The etched PS was further characterized using scanning electron microscope (SEM) imaging and BET measurements. Energetic composites were prepared by impregnating these test strips of PS with sodium, magnesium, or calcium perchlorate salts using methanol solutions. For the heavily doped substrates, this was accomplished by soaking the test strips in the salt solutions for several hours in a humidity controlled chamber continuously purged with dry nitrogen. For the low doped samples, energetic composites were prepared by drop casting a few drops of the oxidizer-methanol solution on the sample surface. The test strips were then mounted on glass slides using double sided adhesive tape and ignited using a 10 ms pulse from a 200 W CO<sub>2</sub> laser. The reactive wave propagation was characterized by means of a high speed video (recorded using a Phantom V 7.3 high speed camera) and a single time integrated (50 ms) spectrum (acquired using an Ocean Optics HR-2000 spectrometer). The temperature of the reactive wave was estimated using a multiwavelength pyrometry algorithm after correcting the collected spectrum for the collection efficiency of the optics.

Controlled microscale structures were created on heavily doped P-type substrates using standard microfabrication techniques. The wafers were patterned using thick positive photoresist (Megaposit SPR-220-7) and etched by deep reactive ion etch (DRIE) using a modified BOSCH process. The photoresist was then stripped off and the wafers were electrochemically etched to create PS. This process results in multiscaled structures with the nanoscale constituent (PS) arranged in controlled micrometer scale patterns. These patterned samples were prepared such that only half the length of the sample contained microscale structures. Samples were ignited in the unpatterned region and the reactive wave was allowed to achieve a steady propagation rate before reaching the patterned region.

## **RESULTS OF NANOPOROUS SILICON EFFORT**

### **Effect of mixture composition on reactive wave propagation**

Using the etch-stop-etch technique, stable porous layers up to 150  $\mu$ m thick were etched on the heavily doped P-type substrates. It was found that PS etched on heavily doped substrates is smooth and uniform, and is stable enough to withstand slight manipulation post impregnation with the oxidizers. In contrast,



the low doped substrates form highly unstable porous layers which disintegrate and explode upon contact. This insensitivity of heavily doped silicon substrates was exploited to clean the surfaces of the samples and gravimetrically determine the oxidizer deposition within the pores. Samples were soaked in solutions of magnesium perchlorate ( $\text{Mg}(\text{ClO}_4)_2$ ), and the amount of oxidizer deposited was controlled by changing the concentration of the oxidizer solutions. The composite equivalence ratio ( $\varphi$ ), is defined as the ratio of the fuel to oxidizer ratio in the mixture, to that of a stoichiometric mixture. Assuming that the void space is completely filled with the oxidizer solution, which upon evaporation deposits the oxidizer in the pores, the theoretical lower bound on the equivalence ratio can be expressed as

$$\varphi_{\min} = \left( \frac{m_{\text{ox}}}{m_f} \right)_{st} \left( \frac{(1-P)\rho_{\text{Si}}}{Ps} \right) \quad (6)$$

where  $P$  is the porosity,  $\rho_{\text{Si}}$  is the density of bulk silicon, and  $s$  is the strength of the solution (g/L). Reactive composites with a wide range of equivalence ratios were prepared using saturated to very dilute solutions of  $\text{Mg}(\text{ClO}_4)_2$  were prepared using PS with a porosity of 0.71 – 0.75 and the reactive wave propagation was studied. It was found that the propagation speeds obtained were always low, between 2 – 8 m/s, with consistent nearly constant spectroscopic temperatures as shown in Table 3. The fuel rich extinction limit was found to be close to  $\varphi_{\min} = 56$  ( $\varphi_{\text{measured}} = 39$ ), at which composition the samples could be ignited but could not sustain a self propagating reaction.

Thermodynamic equilibrium calculations using CHEETAH 4.0 equilibrium code indicate that liquid silicon is one of the major condensed phase species, whose spectral emissivity has a very weak dependence on wavelength. Thus, a gray body approximation was used for the multiwavelength pyrometry algorithm. Also, the thermodynamic calculations indicate that the equilibrium temperature remains nearly constant over a wide range of equivalence ratios as shown in Figure 18. The first sudden drop followed by the plateau in temperature at 2000-2100 K is due to the equilibrium between  $\text{SiO}$  (gas) and liquid  $\text{Si}$  and  $\text{SiO}_2$ . The second drop and plateau is due to the phase change of silicon, which melts at 1683 K.

Table 3: Equivalence ratio, flame propagation speeds and spectroscopically determined temperatures for porous layers etched on heavily doped p-type substrates impregnated with magnesium perchlorate.

S. No.	$\varphi_{\min}$	$\varphi_{\text{measured}}$	$v$ (m/s)	Temperature (K) ( $\epsilon = \text{constant}$ )
1	3.8	1.2-1.24	5-7.7	2044
2	4.6	1.2-3.8	2.6-7.7	1869 - 2184
3	6.7	2.4-3.4	2.5-3.3	1844 - 1930
4	8.3	4.7-5.1	3.9-4.9	1706 - 2043
5	13.5	3.9-5.2	2.4-2.8	1792 - 1870
6	16.5	10.3-19.5	3.2-4.0	2002
7	33.1	20.4-20.8	2.6-3.0	1886 - 1993

The role of the oxidizer used was examined using sodium and calcium perchlorates, which have very different solubilities in methanol. To achieve lower equivalence ratios, saturated solutions of calcium perchlorate ( $\text{Ca}(\text{ClO}_4)_2$ ) in methanol were used to prepare energetic composites. It was found that increasing the oxidizer deposition in the pores reduced the propagation velocity ( $v$ ) despite the mixture composition being closer to stoichiometric. However, using a dilute solution of  $\text{Ca}(\text{ClO}_4)_2$  to prepare composites with the same  $\phi$  as  $\text{NaClO}_4$  resulted in higher  $v$  as shown in Table 2. This indicates that heavily doped substrates which form smooth and uniform porous layers always result in low speed propagations regardless of the oxidizer deposition within the pores. The reduction in  $v$  with increased oxidizer deposition indicates that the reaction is perhaps more strongly controlled by the PS-oxidizer interface than the composition. Increased oxidizer within the pores with a fixed SSA can act as local diluents during the time scales associated with the initial reactive wave, thereby reducing the propagation speed ( $v$ ).

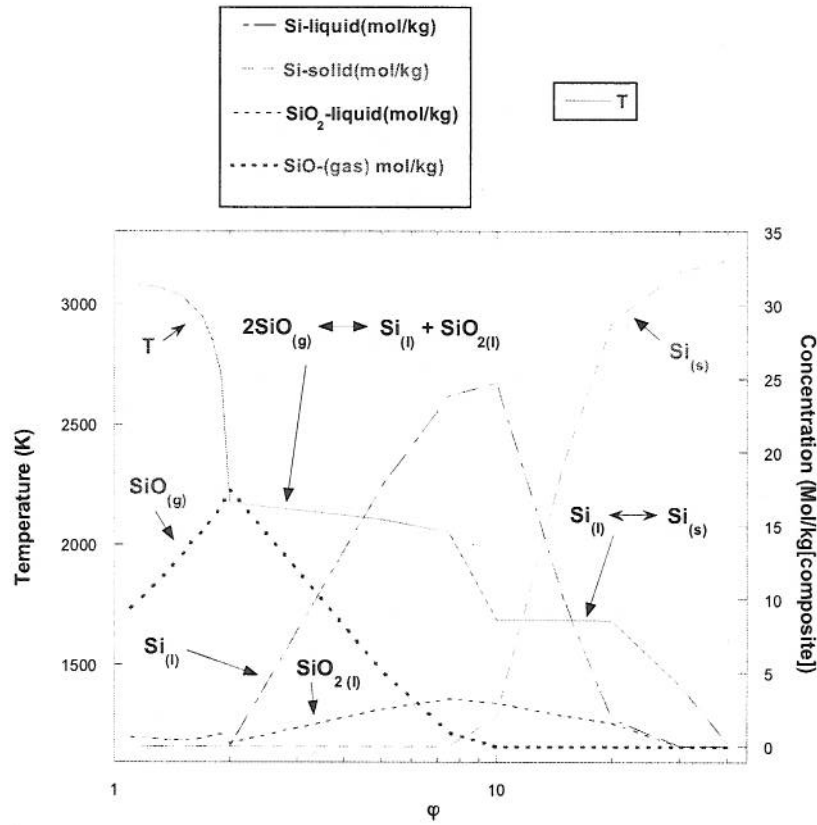


Figure 18: Thermodynamic equilibrium calculations using showing the effect of composite equivalence ratio on reaction zone temperature.

Table 4: Reactive wave propagation as a function of theoretical composite equivalence ratio ( $\phi_{\min}$ ).

Oxidizer solution	$\phi_{\min}$	$v$ (m/s)
$\text{NaClO}_4$	8.32	3.2-3.3
$\text{Ca}(\text{ClO}_4)_2$	7.52	0.7-1.2
$\text{Ca}(\text{ClO}_4)_2$	1.76	4.2-4.3



### Effect of substrate properties

To elucidate the effect of substrate doping levels and the nano and microscale structure on the reactive wave propagation, porous layers were etched on N and P-type substrates with widely different doping levels and impregnated with sodium perchlorate and tested. The heavily doped N and P type substrates yielded porous layers without any micro-crack pattern. The low doped N-type substrates were etched under illumination, and always showed a random micro-crack pattern as shown in Figure 19. The low doped P-type substrates yielded samples with and without a micro-crack pattern. The porous layers etched on all the substrates were impregnated with sodium perchlorate using a saturated solution in methanol. The substrate properties, etch parameters, characteristics, and the reactive wave propagation speeds and temperatures are shown in Table 4.

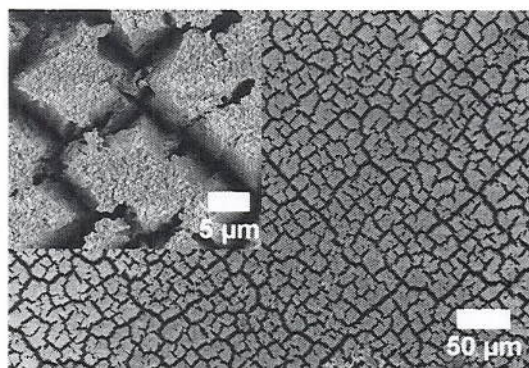


Figure 19: Low doped N-type silicon substrate (2-5  $\Omega$ -cm, Phosphorous doped) showing the random micro-crack pattern formed during the electrochemical etch process.

Table 5: Properties of the substrates and etch parameters used to prepare porous silicon. The porosities were gravimetrically determined, and the surface areas from multi point BET measurement. Gravimetric porosity measurements were not performed on the low doped substrates due to the micro-crack structure and non-uniformities.

Dopant atom	Resistivity ( $\Omega$ -cm)	Current density (mA/cm <sup>2</sup> )	Time (min)	Porosity	SSA (m <sup>2</sup> /g)	$v$ (m/s)	Temperature (K)
(ε = constant)							
Boron	0.001-0.005	40	90	0.6	288	3-3.3	1770-1950
Arsenic	0.001-0.005	60	60	0.62	423	5.4-11.0	2313
Phosphorus	2-5	20	60	-	145	314-372	3208
Boron	10-20	20	30	-	-	4.9	-

The heavily doped N-type substrates exhibited higher flame propagation speeds than the heavily doped P-type substrates indicating the effect of the nanoscale structure and reactivity of the pore surfaces exposed on the reactive wave propagation. The low doped N-type substrates, which yield porous layers with a random micro-crack pattern exhibit high propagation speeds despite their low SSA, indicating that the convective heat transfer at microscopic scales has a stronger effect on the reactive wave propagation than

the nanoscale structure. The low doped P-type substrates were etched and the samples cut from regions without any micro-crack pattern were tested, which showed slow propagations consistent with speeds observed on samples without any micro-crack pattern, providing further proof that the microscale structure is key to achieving high speed propagations.

#### Effect of microscale structure

Standard silicon microfabrication techniques were used to artificially create controlled microscale patterns on heavily doped P-type substrates to exploit the effect of microscale structure and force the propagation from a conductive to a convective mode. Ordered square pillars in the micrometer scale were etched using microfabrication techniques, which was followed by an electrochemical etch to resulting in multiscaled structures as shown in Figure 20. These samples were ignited in the unpatterned region, in which the reactive wave propagated at a slow speed of  $\approx 2$  m/s, consistent with heavily doped substrates without micro-crack patterns. However, upon encountering the patterned region, the reactive wave exhibited a sudden transition to a fast propagating wave with speeds of several hundreds of m/s. These patterned substrates exhibited speeds up to 500 m/s in the patterned region.

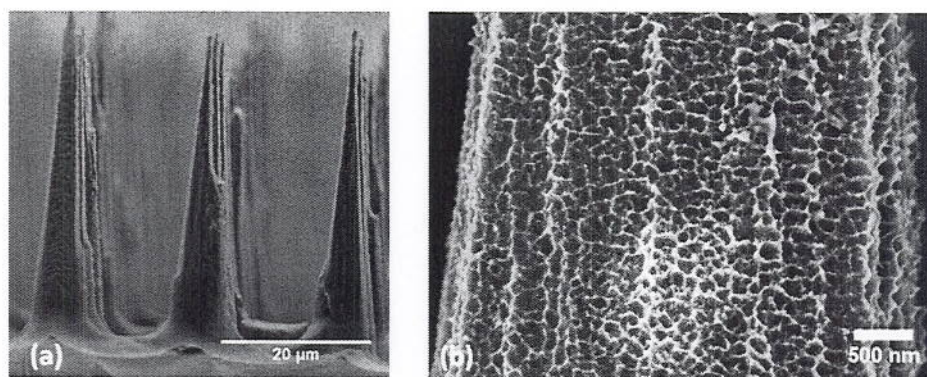


Figure 20: (a) Side view of ordered structures fabricated on heavily doped substrates. The pillars are  $\sim 35 \mu\text{m}$  tall and have  $8 \mu\text{m}$  square bases separated by  $\sim 8 \mu\text{m}$ . (b) SEM image of a single pillar showing the nanoscale features. The nanopores diameters were found to be  $\sim 20$  nm from higher magnification SEM images.

From the various configurations tested of pillared samples tested, the reactive wave was found to be affected the most by gas permeation, spacing between structures and the initial surface area of the microscale patterns. To isolate and study the effect of each of these parameters independently to better understand and control the reactive wave propagation, samples were prepared with plates along the width of the sample normal to the propagation as shown in Figure 21. This configuration eliminates the gas permeation and the spacing and surface area (controlled by the height of the plates) can be independently varied. From these structures, it was found that the initial surface area did not have a strong effect on the gas phase heat transfer, and the gap between the structures was found to have a very strong effect. While gaps of  $25 \mu\text{m}$  resulted in no transition,  $15 \mu\text{m}$  gaps accelerated the reactive wave from 4 m/s to 6 m/s whereas  $5 \mu\text{m}$  gaps resulted in a transition from 4 m/s to 30 m/s. Such multiscaled structures can be used to design energetic materials with precisely controlled energy release profiles, making PS a suitable nEM for a range of micropyrrotechnic applications.



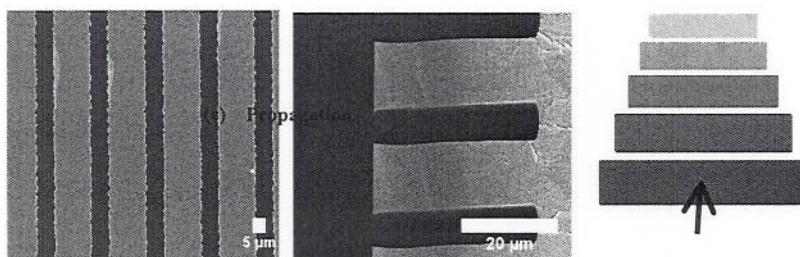


Figure 21: Microscale patterns etched on heavily doped P-type substrates. (a) and (b) Top and side views showing 15  $\mu\text{m}$  plates with a spaced 5  $\mu\text{m}$  apart. (c) Direction of reactive wave propagation relative to the plate orientation.

## Mechanically Activated Si and Si-Al Reactives

In this final period of this project we have obtained some initial results involving mechanically activated (MA) silicon reactives and silicon-aluminum reactives. Micron sized Si/PTFE mixtures (stoichiometric) - 325 mesh Si and 12  $\mu\text{m}$  PTFE milled together. No differences were observed in qualitative reactivity tests between high intensity milled and physically mixed. The high tensile strength ( $\sim 7\text{GPa}$ ) makes MA ineffective. However, we were able to obtain promising reactivity results using a two-step milling process. Specifically, a cryomilling step was first applied to reduce and refine the powders, followed by high intensity (SPEX) milling to consolidate the mixture. The difference was quantified in DSC/TGA measurements shown in Figure 22. The two-step milling clearly shows a Si-PTFE exotherm, as noted on the figure.

AlSi alloys have also been considered because they are more ductile than Si, and the eutectic composition has lower melting point than neat Al or Si (e.g., AlSi ( $\sim 12.6\%$  Si),  $T_m \sim 577^\circ\text{C}$  vs.  $660^\circ\text{C}$  for Al). Hypereutectic compositions (AlSi(40% Si) and AlSi (50% Si)) were also investigated. We found these mixtures to have improved sensitivity over nanoaluminum materials (see Table 6). Initial results indicate that MA of Si reactives can alter ignition characteristics dramatically and allows use of micron-sized particles with increased reactivity (instead of nanoscale materials). The materials can be tailored with inexpensive pre-cursor materials. The AlSi eutectic and hypereutectic materials interesting alternative to neat Al or Si and the altered properties (melting point and ductility) of the AlSi mixtures lead to more effective milling and reactivity than with Si only. Although this project is ending a fellowship student will continue this work and we expect to publish results on this and plan to submit a patent disclosure.

Table 6: Electrostatic sensitivity of AlSi reactives.

Mixture	Mill Time (min)	ESD
50 nm Novacentrix Al	0	1.1 mJ
70/30 AlSi(12%Si)/PTFE	20	875 mJ
	40	71 mJ
	60	37 mJ
	20	71 mJ
70/30 AlSi(40%Si)/PTFE	20	71 mJ

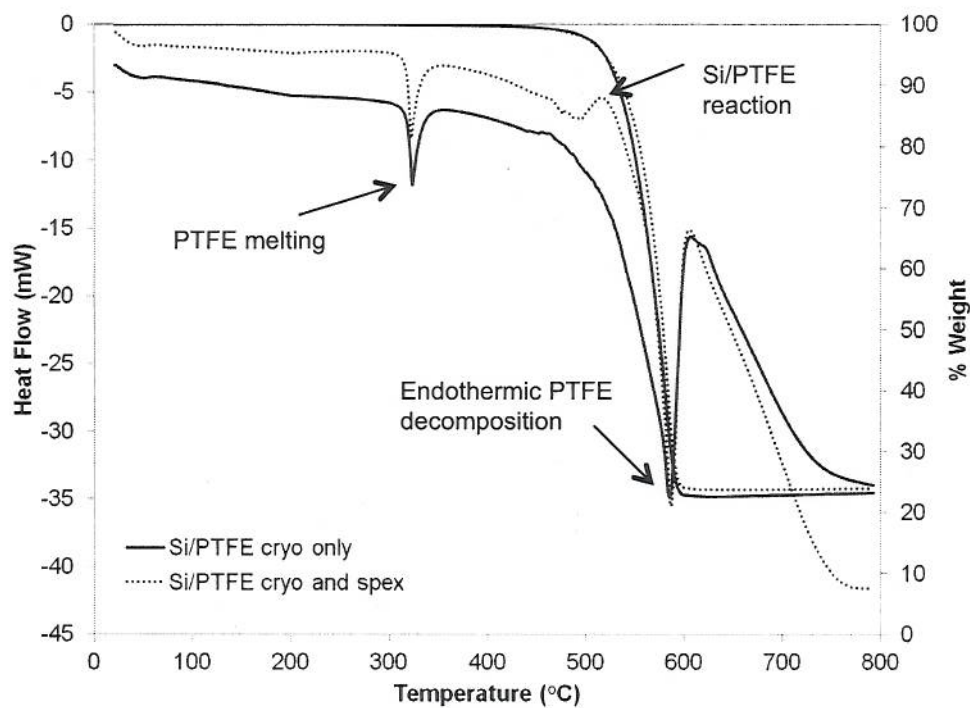


Figure 22: DSC and TGA traces for mechanically activated Si-PTFE.



**DISTRIBUTION LIST  
DTRA-TR-13-1**

**DEPARTMENT OF DEFENSE**

DEFENSE TECHNICAL  
INFORMATION CENTER  
8725 JOHN J. KINGMAN ROAD,  
SUITE 0944  
FT. BELVOIR, VA 22060-6201  
ATTN: DTIC/OCA

**DEPARTMENT OF DEFENSE  
CONTRACTORS**

EXELIS, INC.  
1680 TEXAS STREET, SE  
KIRTLAND AFB, NM 87117-5669  
ATTN: DTRIAC